Journal of the Physical Society of Japan **92**, 012001 (2023) **Invited Review Papers**
https://doi.org/10.7566/JPSJ.92.012001

First-principles Phonon Calculations with Phonopy and Phono3py

Atsushi Togo[1,2*]

[1]*Research and Services Division of Materials Data and Integrated System, National Institute for Materials Science, Tsukuba, Ibaraki 305-0047, Japan*
[2]*Center for Elements Strategy Initiative for Structural Materials, Kyoto University, Sakyo, Kyoto 606-8501, Japan*

(Received July 31, 2022; accepted October 17, 2022; published online December 6, 2022)

Harmonic, quasi-harmonic, and anharmonic phonon properties of crystals are getting to be better predicted using first-principles phonon calculations by virtue of the progress of the calculation methods and increasing computer power. In this review, basic formulae of phonon properties are reviewed with the phonon calculation examples performed using the phonon calculation codes, phonopy and phono3py, combined with the first-principles calculations. The computational workflow to utilize the first-principles phonon calculation is straightforward and its automation is of great interest to science. Therefore, a few practical applications of the automated first-principles phonon calculations are also presented.

CONTENTS

1. Introduction 1
2. Crystal Structure and Potential 3
3. Harmonic Phonon Calculation 3
3.1 Normal coordinates 3
3.2 Dynamical matrix 4
3.3 Phonon coordinates 4
3.4 Supercell model 5
3.5 Non-analytical term correction 6
3.6 Density of states 7
3.7 Atomic displacements at finite temperatures 7
3.8 Dynamic structure factor 8
3.9 Thermal properties at constant volume 8
3.10 Phonon group velocity 8
3.11 Irreducible representation 9
4. Quasi-harmonic Phonon Calculation 9
4.1 Mode Grüneisen parameter 9
4.2 Thermal expansion 9
4.3 Structural phase transition under shear strain 10
5. Anharmonic Phonon Calculation 11
5.1 Phonon coordinate transformation 11
5.2 Phonon lifetime 12
5.3 Phonon spectral function 12
6. Lattice Thermal Conductivity Calculation 13
6.1 Relaxation time approximation 13
6.2 Phonon-isotope scattering 15
6.3 Direct solution to linearized phonon Boltzmann equation 15
7. Automation of First-principles Phonon Calculations 16
7.1 First-principles phonon calculation workflow 17
7.2 Automated phonon calculation workflow 17
7.3 Iteration of harmonic phonon calculations 18
7.4 Execution of many phonon calculations 19
7.5 Recursive search of phase transition pathways 19
8. Summary 20
Acknowledgments 20
References 20

1. Introduction

In crystals, atoms vibrate collectively. The collective atomic motions are often described by phonons. Since phonons are ubiquitous, understanding phonons is required in every research of crystals. Phonons are measured by Raman and infrared (IR) spectroscopies that are used to observe phonon spectra near the origin of reciprocal space. Inelastic neutron and X-ray scatterings can measure the phonon spectra at general points in reciprocal space, although they require large-scale facilities for the use. Each phonon measurement technique has each advantage, and they are used as complemental techniques. In addition to these experimental tools, phonon calculation is another complemental tool of the phonon measurement.

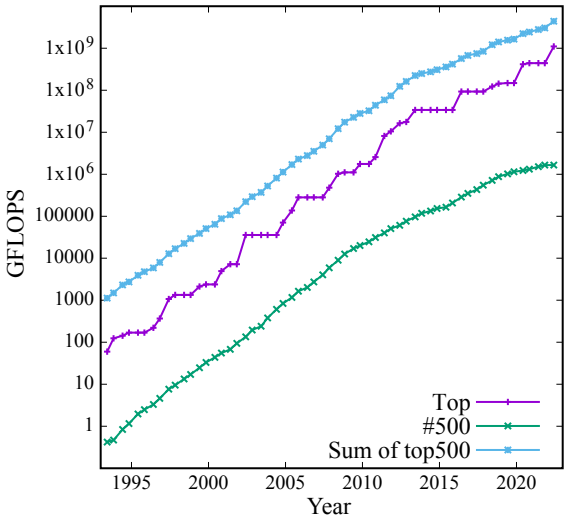

Fig. 1. (Color online) The 500 most powerful non-distributed computer systems in the world from the TOP500 project.[7,8)]

The phonon calculation is used for a variety of research purposes due to its high predictability. Thermal properties such as heat capacity, thermal expansion, and thermal conductivity are well predicted by using it. Systematic data of phonon properties can be generated by the high-throughput phonon calculation.

Our computer power has been growing exponentially for many years as shown in Fig. 1. Utilizing massive computer power, significant theoretical predictions will be achieved by computer simulations. In solid state physics, the computer simulation solving electronic Schödinger equation, which is called first-principles calculation, has become of practical use by great amount of efforts of many researchers and engineers in this and last centuries.[1)] Increasing computer power

brought the first-principles calculation being developed toward more accurate calculations, larger scale calculations, and high-throughput calculations. Strongly assisted by user-friendly software packages, e.g., the VASP[2–4] and QuantumEspreesso[5,6] codes and many more, the first-principles calculation is used as a routine tool for a variety of purposes in different fields of science and industry.

Progress of the first-principles calculations and growth of computer power in the last decades enabled us to perform the phonon calculations based on the first-principles calculation. Phonon properties predicted by first-principles phonon calculation are often in good agreements with experimental results, and the first-principles phonon calculation is now recognized as a routine tool in science and engineering. The required computational demand is reasonably small at the harmonic and quasi-harmonic approximations for the current computer power. The operation of the calculations is straightforward even for non-specialists of theoretical calculations with the aid of user-friendly simulation codes.

Accurate phonon calculation requires accurate derivatives of crystal potential with respect to atomic displacements that are called force constants. Until the first-principles calculation became usable as the simulation engine, it had been difficult to obtain accurate force constants in a systematic way. For the predictive accuracy, the phonon calculation relies on the first-principles calculation indispensably. In the majority of cases, the density functional theory (DFT)[9,10] is used as the first-principles calculation for the phonon calculation.

There are two popular types of the first-principles phonon calculations: finite-displacement supercell approach and density-functional perturbation theory (DFPT).[11–16] Difference of their computational procedures is presented briefly in Fig. 2. In the finite-displacement supercell approach, the first-principles calculation is used as the engine to obtain atomic forces in supercell crystal structure model. The force constants are calculated from sufficient number of supercells with different sets of displacements and respective forces obtained by the first-principles calculation. The detailed computational workflow is presented in Sect. 7.1. The phonons are calculated exactly (i.e., without interpolation) from the supercell force constants at the wave vectors commensurate with the supercell shape with respect to the primitive cell. At the other wave vectors, phonons are obtained as interpolated results. In practice, use of the supercell size with a few hundred atoms often gives reasonable phonon results by the interpolation, although the required accuracy depends on the calculation purposes. The details of this approach are described in Sect. 3.4.

In the DFPT approach, force constants are exactly calculated in reciprocal space at arbitrary wave vectors by solving the variation of the Kohn–Sham orbitals. Optionally, direct-space force constants similar to the supercell force constants are computed by the Fourier transform from the reciprocal-space force constants sampled on a regular grid.[15] The force constants in direct space are again Fourier transformed to those in reciprocal space at arbitrary wave vectors. This technique may be called Fourier interpolation.

Normally, users choose the phonon calculation approach following the research purpose and computational environment. Using the finite-displacement supercell approach, accessible exact wave vectors are limited to those commensurate points of the supercell shape. It means that, to calculate phonons near Γ point exactly, a huge supercell is necessary and it requires large computational demand or usually impractical. Using DFPT, phonons at any wave vectors are calculated exactly. By the same computational reason, DFPT is advantageous or only practically possible in dense sampling of exact wave vectors in the reciprocal space. This is especially important for the system where the Fourier interpolation poorly works. A practical advantage of the finite-displacement supercell approach is in the fact that atomic force calculations for a variety of exchange–correlation functionals, pseudo-potential methods, and beyond-DFT approaches are implemented in popular first-principles calculation codes, however, it may not be the case for DFPT implementations.

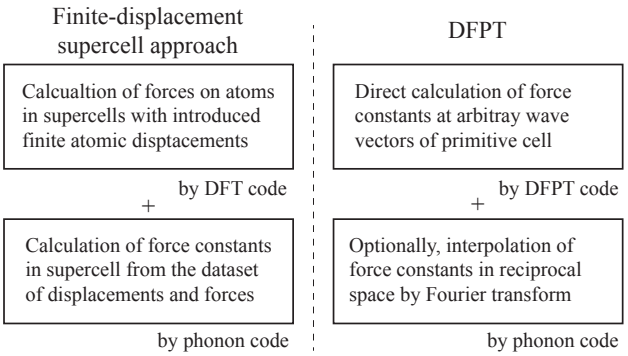

Fig. 2. Computational procedures of force constants by finite-displacement supercell approach and DFPT.

At the level of the harmonic and quasi-harmonic approximations, the first-principles phonon calculation has became a routine tool for research. It is widely used not only in scientific community but also for engineering purpose. Many researchers or engineers would be able to find computational resources to perform it. The community of the phonon calculation grows constantly. There are a wide variety of the phonon calculation codes, e.g., in the finite-displacement supercell approach, the PHONON,[17] PHON,[18] ALAMODE,[19–21] YPHON,[22] TDEP,[23–25] and phonopy[26] codes, and in DFPT, the Quantum ESPRESSO, Abinit,[27–29] and ELK[30] codes. The VASP code implements the both approaches at Γ point. Each code has its specialty and advantage and users choose the codes following their own purposes.

Efforts payed on scientific software development and modern computing power allowed us to perform lattice thermal conductivity (LTC) calculation from the Peierls–Boltzmann equation[31–34] based on the first-principles phonon calculation. This enabled us to predict thermal conductivity of nonmagnetic insulators at reasonable accuracy as presented in Sect. 6. There are several software packages for this type of the LTC calculations, e.g., ALAMODE, TDEP, ShengBTE,[35] almaBTE,[36] PhonTS,[37] and phono3py.[38]

Self-consistent phonon calculation is necessary for strongly anharmonic crystals. In the last decade, active research has been made in this field,[20,25,39] and a variety of the methods have been developed. Software packages that implement those methods are available in the codes such as the SCAILD,[40] ALAMODE, TDEP, QSCAILD,[41] and SSCHA[39,42–45] codes. An example is presented in Sect. 7.3.

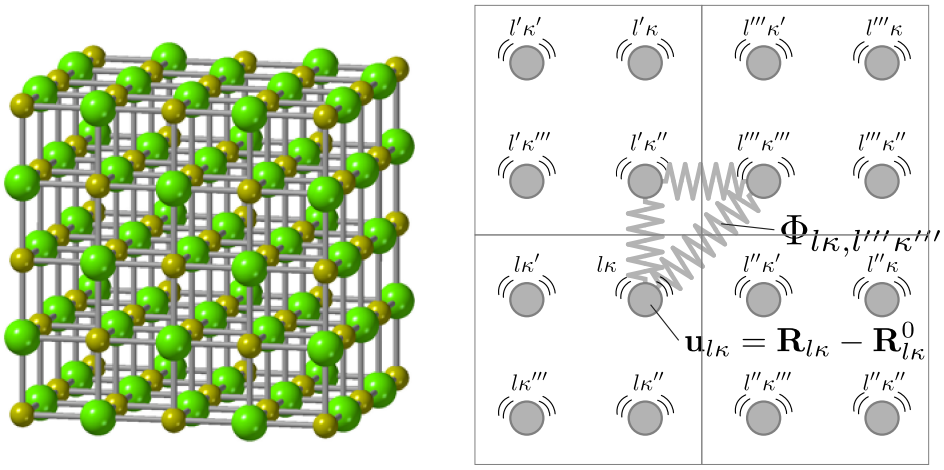

Fig. 3. (Color online) Crystal structure model and interacting atoms vibrating in the vicinity of their equilibrium positions $\mathbf{R}^0_{l\kappa}$. The atomic positions $\mathbf{R}_{l\kappa}$ deviate from their equilibrium positions due to vibrations, which is described by displacements $\mathbf{u}_{l\kappa} = \mathbf{R}_{l\kappa} - \mathbf{R}^0_{l\kappa}$. In the Taylor series expansion of crystal potential with respect to the displacements of Eq. (1), the expansion coefficients ($\Phi_{lk\alpha,l'k'\alpha',\ldots}$) are viewed as generalized spring constants among atoms.

Although force-constants calculation has been provided as a feature of each phonon code, a few software packages such as the ALM[46] and hiPhive[47] codes have been developed specifically for the force-constants calculation. These codes have a variety of advanced features and modern accessibility as software libraries to be usable from phonon calculation codes. One of the aims of these codes is to calculate anharmonic force constants efficiently. The other important feature is to calculate force constants at finite temperatures introducing finite atomic displacements beyond small displacement regime (See Sect. 7.3).

In this review, computational approaches of the first-principles phonon calculations are explained for research applications at different levels of approximations. Although the basic theory of phonons are described for the use of explanation, it is recommended to refer the excellent books (e.g., Refs. 33, 34, 48–52) to learn the physics of phonons in depth, where vital theoretical and mathematical insights are found. Notably, symmetry properties of phonons are insightful,[49,53–55] but are omitted in this review.

In the following sections, formulae and methods implemented in the phonopy and phono3py codes are presented along with associated calculation examples. In Sect. 2, crystal model and crystal potential used for the phonon calculation are described. In Sect. 3, to define phonons, transformation of atomic vibrations from direct coordinates to phonon coordinates is introduced. Then finite-displacement supercell approach and a variety of harmonic phonon properties are presented. Some numerical techniques are covered briefly in this section. In Sect. 4, quasi-harmonic approximations (QHA) and its applications are presented. Thermal expansion is treated in this section. In Sect. 5, phonon–phonon interaction as anharmonic phonon calculation is described. Using the result of the phonon–phonon interaction calculations, LTC calculations and some means to analyze the results are presented in Sect. 6. Since intelligent use of huge computing power is important for us, a computational workflow of a typical phonon calculation is explained in Sect. 7. High-throughput phonon calculation and particular algorithms employed for the studies are presented as use cases of automated phonon calculation workflows.

2. Crystal Structure and Potential

A crystal in the phonon calculation is treated as a physical model where equilibrium positions of atoms are arranged on the crystal lattice under the periodic boundary condition. In this model, atoms vibrate in the vicinity of their equilibrium positions as illustrated in Fig. 3. The crystal structure is represented by basis vectors of a unit cell at the lattice point l and equilibrium positions of atoms labeled by κ in each unit cell. The atoms are indexed compositely by $l\kappa$ and their equilibrium positions are denoted as $\mathbf{R}^0_{l\kappa}$. The number of unit cells in a crystal and the number of atoms in each unit cell are denoted by N and n_a, respectively. V_c is used to mean the volume of the unit cell. NV_c gives the volume of the crystal.

Atomic positions $\mathbf{R}_{l\kappa}$ deviate from their equilibrium positions $\mathbf{R}^0_{l\kappa}$ by vibrations. The deviations are measured by displacements $\mathbf{u}_{l\kappa} = \mathbf{R}_{l\kappa} - \mathbf{R}^0_{l\kappa}$. With respect to the displacements, potential energy of crystal $\mathscr{V}$ may be expanded into a Taylor series:

$$\begin{aligned}\mathscr{V} &= \Phi_0 + \mathscr{H}_1 + \mathscr{H}_2 + \mathscr{H}_3 + \cdots \\ &= \Phi_0 + \sum_{l\kappa\alpha} \Phi_{l\kappa\alpha} u_{l\kappa\alpha} \\ &\quad + \frac{1}{2} \sum_{l\kappa\alpha,l'\kappa'\alpha'} \Phi_{l\kappa\alpha,l'\kappa'\alpha'} u_{l\kappa\alpha} u_{l'\kappa'\alpha'} \\ &\quad + \frac{1}{3!} \sum_{l\kappa\alpha,l'\kappa'\alpha',l''\kappa''\alpha''} \Phi_{l\kappa\alpha,l'\kappa'\alpha',l''\kappa''\alpha''} u_{l\kappa\alpha} u_{l'\kappa'\alpha'} u_{l''\kappa''\alpha''} + \cdots,\end{aligned} \tag{1}$$

where α denotes the Cartesian index, and the coefficients of the series expansion, Φ_0, $\Phi_{l\kappa\alpha}$, $\Phi_{l\kappa\alpha,l'\kappa'\alpha'}$ $\Phi_{l\kappa\alpha,l'\kappa'\alpha',l''\kappa''\alpha''}$, are the zero-th, first, second, and third order force constants, respectively. $\Phi_{l\kappa\alpha} = 0$ are assumed because $\mathbf{u}_{l\kappa}$ are measured from their equilibrium positions, and $\Phi_0 = 0$ is chosen in the next section.

3. Harmonic Phonon Calculation

3.1 Normal coordinates

The phonon calculation is based on a lattice model of interacting atoms as illustrated in Fig. 3. Normal coordinates are convenient to describe the system, which may be

introduced as follows. In the harmonic approximation with $\Phi_{l\kappa\alpha,l'\kappa'\alpha'} = \frac{\partial^2 \mathscr{V}}{\partial u_{l\kappa\alpha}\partial u_{l'\kappa'\alpha'}}$ and ignoring higher order terms $\Phi_{l\kappa\alpha,l'\kappa'\alpha',l''\kappa''\alpha'',\cdots} \equiv 0$, the energy of vibrating atoms are written as

$$\begin{aligned}\mathscr{H}_{\rm ha} &= \mathscr{T} + \mathscr{H}_2 \\ &= \sum_{l\kappa\alpha}\frac{1}{2}m_\kappa\left(\frac{du_{l\kappa\alpha}}{dt}\right)^2 \\ &\quad + \frac{1}{2}\sum_{l\kappa\alpha,l'\kappa'\alpha'} u_{l\kappa\alpha}\Phi_{l\kappa\alpha,l'\kappa'\alpha'}u_{l'\kappa'\alpha'},\end{aligned} \tag{2}$$

where m_κ gives the atomic mass. Defining mass normalized displacement $\tilde{u}_{l\kappa\alpha} = \sqrt{m_\kappa}u_{l\kappa\alpha}$, Eq. (2) is rewritten as

$$\begin{aligned}\mathscr{H}_{\rm ha} &= \sum_{l\kappa\alpha}\frac{1}{2}\left(\frac{d\tilde{u}_{l\kappa\alpha}}{dt}\right)^2 \\ &\quad + \frac{1}{2}\sum_{l\kappa\alpha,l'\kappa'\alpha'}\tilde{u}_{l\kappa\alpha}\left(\frac{1}{\sqrt{m_\kappa}}\Phi_{l\kappa\alpha,l'\kappa'\alpha'}\frac{1}{\sqrt{m'_\kappa}}\right)\tilde{u}_{l'\kappa'\alpha'}.\end{aligned} \tag{3}$$

Looking at the reduced force constants $\tilde{\Phi}_{l\kappa\alpha,l'\kappa'\alpha'} = \frac{1}{\sqrt{m_\kappa}}\Phi_{l\kappa\alpha,l'\kappa'\alpha'}\frac{1}{\sqrt{m_{\kappa'}}}$ as a square matrix $\tilde{\Phi}$, since $\tilde{\Phi}$ is a symmetric matrix, it is diagonalized as

$$\tilde{\Phi} = \mathrm{U}\Omega^2\mathrm{U}^\top, \tag{4}$$

where $\Omega^2 = \mathrm{diag}(\cdots,\omega_\xi^2,\cdots)$ and U is the orthogonal matrix whose columns are the eigenvectors $w_{l\kappa\alpha}(\xi)$. ξ denotes the index of the normal mode. Equation (2) is rewritten in the matrix notation with introducing the column matrix $\tilde{\mathbf{u}} = (\sqrt{m_\kappa}u_{l\kappa\alpha}\ \cdots)^\top$ as

$$\begin{aligned}\mathscr{H}_{\rm ha} &= \frac{1}{2}\dot{\tilde{\mathbf{u}}}^\top\dot{\tilde{\mathbf{u}}} + \frac{1}{2}\tilde{\mathbf{u}}^\top\tilde{\Phi}\tilde{\mathbf{u}} \\ &= \frac{1}{2}(\mathrm{U}^\top\dot{\tilde{\mathbf{u}}})^\top(\mathrm{U}^\top\dot{\tilde{\mathbf{u}}}) + (\mathrm{U}^\top\tilde{\mathbf{u}})^\top\Omega^2(\mathrm{U}^\top\tilde{\mathbf{u}}) \\ &= \frac{1}{2}\dot{\mathbf{Q}}^\top\dot{\mathbf{Q}} + \frac{1}{2}\mathbf{Q}^\top\Omega^2\mathbf{Q},\end{aligned} \tag{5}$$

where $\mathbf{Q}$ gives the normal coordinates defined by $\tilde{\mathbf{u}} = \mathrm{U}\mathbf{Q}$ and the dot on $\tilde{\mathbf{u}}$ and $\mathbf{Q}$ means the time derivative.

3.2 Dynamical matrix

The eigenvalue problem of Eq. (4) is written explicitly as

$$\sum_{l'\kappa'\alpha'}\tilde{\Phi}_{l\kappa\alpha,l'\kappa'\alpha'}w_{l'\kappa'\alpha'}(\xi) = \omega_\xi^2 w_{l\kappa\alpha}(\xi). \tag{6}$$

By the Bloch theorem, the eigenvector $w_{l\kappa\alpha}(\xi)$ of the wave vector $\mathbf{q}$ is written as[33,50]

$$w_{l\kappa\alpha,\mathbf{q}}(\xi) = \frac{1}{\sqrt{N}}W_{\kappa\alpha}(\xi)e^{i\mathbf{q}\cdot\mathbf{R}^0_{l\kappa}}, \tag{7}$$

where $W_{\kappa\alpha}(\xi)$ is a periodic function of the crystal lattice. In Eq. (7), the factor $\frac{1}{\sqrt{N}}$ normalizes $W_{\kappa\alpha}(\xi)$ so that $\sum_{\kappa\alpha}|W_{\kappa\alpha}(\xi)|^2 = 1$. Substituting Eq. (7) into Eq. (6), multiplying both sides of Eq. (6) by $e^{-i\mathbf{q}\cdot\mathbf{R}^0_{l\kappa}}/\sqrt{N}$, and summing over l on both sides of the equation to get

$$\sum_{\kappa'\alpha'}D_{\kappa\alpha,\kappa'\alpha'}(\mathbf{q})W_{\kappa'\alpha'}(\mathbf{q}\nu) = \omega_{\mathbf{q}\nu}^2 W_{\kappa\alpha}(\mathbf{q}\nu), \tag{8}$$

where ξ is replaced by the composite index $\mathbf{q}\nu$ of the phonon modes, and

$$\begin{aligned}D_{\kappa\alpha,\kappa'\alpha'}(\mathbf{q}) &= \sum_{ll'}\frac{e^{-i\mathbf{q}\cdot\mathbf{R}^0_{l\kappa}}}{\sqrt{N}}\tilde{\Phi}_{l\kappa\alpha,l'\kappa'\alpha'}\frac{e^{i\mathbf{q}\cdot\mathbf{R}^0_{l'\kappa'}}}{\sqrt{N}} \\ &= \frac{1}{N\sqrt{m_\kappa m_{\kappa'}}}\sum_{ll'}\Phi_{l\kappa\alpha,l'\kappa'\alpha'}e^{i\mathbf{q}\cdot(\mathbf{R}^0_{l'\kappa'}-\mathbf{R}^0_{l\kappa})} \\ &= \frac{1}{\sqrt{m_\kappa m_{\kappa'}}}\sum_{l'}\Phi_{0\kappa\alpha,l'\kappa'\alpha'}e^{i\mathbf{q}\cdot(\mathbf{R}^0_{l'\kappa'}-\mathbf{R}^0_{0\kappa})}.\end{aligned} \tag{9}$$

$D_{\kappa\alpha,\kappa'\alpha'}(\mathbf{q})$ is the dynamical matrix. In Eq. (8), ν of $\mathbf{q}\nu$ denotes the phonon band index. In the last equation of Eq. (9), lattice translational symmetry of the force constants was used. Note that the definition of the dynamical matrix in Eq. (9) (C-type[34]) is used throughout this review although several different definitions are available in literature. Another popular definition (D-type[34]) uses the phase factor by the distance between lattice points as follows:

$$D^{\text{D-type}}_{\kappa\alpha,\kappa'\alpha'}(\mathbf{q}) = \frac{1}{\sqrt{m_\kappa m_{\kappa'}}}\sum_{l'}\Phi_{0\kappa\alpha,l'\kappa'\alpha'}e^{i\mathbf{q}\cdot(\mathbf{R}^0_{l'}-\mathbf{R}^0_0)}. \tag{10}$$

These two dynamical matrices are mutually related by a unitary transformation, therefore, their eigenvalues ($\omega^2_{\mathbf{q}\nu}$) are the same, but their eigenvectors are different by phase factors as follows:

$$W^{\text{D-type}}_{\kappa\alpha}(\mathbf{q}\nu) = W_{\kappa\alpha}(\mathbf{q}\nu)e^{i\mathbf{q}\cdot\mathbf{R}^0_{0\kappa}}, \tag{11}$$

where $W^{\text{D-type}}_{\kappa\alpha}(\mathbf{q}\nu)$ is an eigenvector of $D^{\text{D-type}}_{\kappa\alpha,\kappa'\alpha'}(\mathbf{q})$.

3.3 Phonon coordinates

In practice, the eigenvalue problem of Eq. (8) is solved using a linear algebra solver, e.g., LAPACK[56] or its convenient interface such as numpy,[57] for which $D_{\kappa\alpha,\kappa'\alpha'}(\mathbf{q})$ is arranged in a $3n_\mathrm{a}\times 3n_\mathrm{a}$ matrix $\mathrm{D}(\mathbf{q})$ as illustrated in Fig. 4. Since $\mathrm{D}(\mathbf{q})$ is an Hermitian matrix, i.e., $\mathrm{D}^\dagger(\mathbf{q}) = \mathrm{D}(\mathbf{q})$, it is diagonalizable with real eigenvalues $\omega^2_{\mathbf{q}\nu}$ similarly to Eq. (4),

$$\mathrm{D}(\mathbf{q}) = \mathrm{U}(\mathbf{q})\Omega^2(\mathbf{q})\mathrm{U}^\dagger(\mathbf{q}). \tag{12}$$

In Eq. (12), $\mathrm{U}(\mathbf{q})$ is the unitary matrix whose columns are the eigenvectors $W_{\kappa\alpha}(\mathbf{q}\nu)$, and $\Omega^2(\mathbf{q}) = \mathrm{diag}(\cdots,\omega^2_{\mathbf{q}\nu},\cdots)$ where $\omega_{\mathbf{q}\nu}$ is the phonon frequency. The matrix $\mathrm{D}(\mathbf{q})$ is positive definite (at $\mathbf{q}=\mathbf{0}$ positive semi-definite) if the crystal is dynamically stable. Otherwise, the crystal should exhibit spontaneous structural transition by breaking the crystal symmetry. The dynamical stability can be examined by $\omega_{\mathbf{q}\nu}$. Any imaginary phonon frequency indicates structural instability.

From $\tilde{\mathbf{u}} = \mathrm{U}\mathbf{Q}$ in Eqs. (5) and (7), the displacement is written as

$$u_{l\kappa\alpha} = \frac{1}{\sqrt{Nm_\kappa}}\sum_{\mathbf{q}\nu}Q(\mathbf{q}\nu)W_{\kappa\alpha}(\mathbf{q}\nu)e^{i\mathbf{q}\cdot\mathbf{R}^0_{l\kappa}}, \tag{13}$$

where $Q(\mathbf{q}\nu)$ are the phonon coordinates. Using phonon creation ($a^\dagger_{\mathbf{q}\nu}$) and annihilation ($a_{\mathbf{q}\nu}$) operators, the solution of the harmonic oscillator problem[58] suggests $Q(\mathbf{q}\nu)$ to be represented by[50,51]

$$Q(\mathbf{q}\nu) = \sqrt{\frac{\hbar}{2\omega_{\mathbf{q}\nu}}}(a_{\mathbf{q}\nu} + a^\dagger_{-\mathbf{q}\nu}), \tag{14}$$

where $\hbar$ is the reduced Planck constant. The harmonic Hamiltonian is transformed to be written by using $a^\dagger_{\mathbf{q}\nu}$ and $a_{\mathbf{q}\nu}$ as a sum over all phonon modes,[33,50,51]

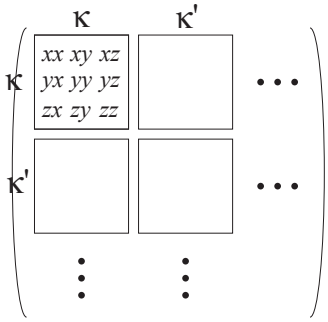

Fig. 4. Dynamical matrix represented in a matrix shape of $3n_a \times 3n_a$. This square matrix is readily diagonalizable using a linear algebra solver, e.g., LAPACK,[56] or its convenient interface such as numpy.[57]

$$\mathscr{H}_{\mathrm{ha}} = \sum_{\mathbf{q}\nu} \hbar\omega_{\mathbf{q}\nu} \left(a^{\dagger}_{\mathbf{q}\nu} a_{\mathbf{q}\nu} + \frac{1}{2} \right). \tag{15}$$

Statistical average of phonon occupation number of each phonon mode known as the Bose–Einstein distribution is given by

$$n_{\mathbf{q}\nu}(T) = \langle a^{\dagger}_{\mathbf{q}\nu} a_{\mathbf{q}\nu} \rangle = \frac{1}{e^{\frac{\hbar\omega_{\mathbf{q}\nu}}{k_{\mathrm{B}}T}} - 1} = \frac{1}{2e^{\frac{\hbar\omega_{\mathbf{q}\nu}}{2k_{\mathrm{B}}T}} \sinh \frac{\hbar\omega_{\mathbf{q}\nu}}{2k_{\mathrm{B}}T}}, \tag{16}$$

where k_{B} and T are the Boltzmann constant and temperature, respectively. Using Eq. (16), harmonic phonon energy is obtained as

$$\langle \mathscr{H}_{\mathrm{ha}} \rangle = \sum_{\mathbf{q}\nu} \hbar\omega_{\mathbf{q}\nu} \left(n_{\mathbf{q}\nu} + \frac{1}{2} \right). \tag{17}$$

3.4 Supercell model

With the atomic forces and small displacements, the harmonic force constants $\Phi_{l\kappa\alpha,l'\kappa'\alpha'}$ are obtained by solving simultaneous linear-equations:[17]

$$-f_{l\kappa\alpha} = \sum_{l'\kappa'\alpha'} \Phi_{l\kappa\alpha,l'\kappa'\alpha'} u_{l'\kappa'\alpha'}. \tag{18}$$

In the finite-displacement supercell approach, supercell model is employed to calculate force constants in Eq. (18). The supercell is built by integer linear-combination of basis vectors of the primitive cell. More precisely, the basis vectors of the primitive cell, $(\mathbf{a}_{\mathrm{p}}, \mathbf{b}_{\mathrm{p}}, \mathbf{c}_{\mathrm{p}})$, is transformed by an integer matrix $\mathrm{P}_{\mathrm{p}\to\mathrm{s}}$ having positive determinant to those of the supercell, $(\mathbf{a}_{\mathrm{s}}, \mathbf{b}_{\mathrm{s}}, \mathbf{c}_{\mathrm{s}})$, as

$$(\mathbf{a}_{\mathrm{s}}, \mathbf{b}_{\mathrm{s}}, \mathbf{c}_{\mathrm{s}}) = (\mathbf{a}_{\mathrm{p}}, \mathbf{b}_{\mathrm{p}}, \mathbf{c}_{\mathrm{p}})\mathrm{P}_{\mathrm{p}\to\mathrm{s}}. \tag{19}$$

In the supercell, one or multiple atoms are displaced, and the forces on all atoms in the supercell are calculated using the first-principles calculation. As an example shown in Fig. 5, one atom is displaced in a supercell. The supercell contains $|\mathrm{P}_{\mathrm{p}\to\mathrm{s}}|$ primitive cells. The periodicity inside the supercell is broken by the displacement as shown in Fig. 5(a). In the first-principles calculation for solids, the supercell model is the unit of the periodicity as shown in Fig. 5(b), and forces of all atoms in the supercell are calculated under the system where each mirror image of the supercell contains the same displacement. The force of each atom is obtained as the response of the all displacements.

Sufficient number of supercells with different configurations of displacements and their calculated forces are required as a dataset to solve Eq. (18) so that the degrees of freedom of the force constants are fulfilled. Thus obtained force constants are called supercell force constants. The degrees of freedom of the supercell force constants are reduced utilizing various symmetries. This means that required number of supercells with displacements is also reduced. In typical DFT calculations, all atomic forces in a supercell are obtained by small additional computation from the converged Kohn–Sham orbitals.[1] This is a useful feature of quantum mechanical calculations.

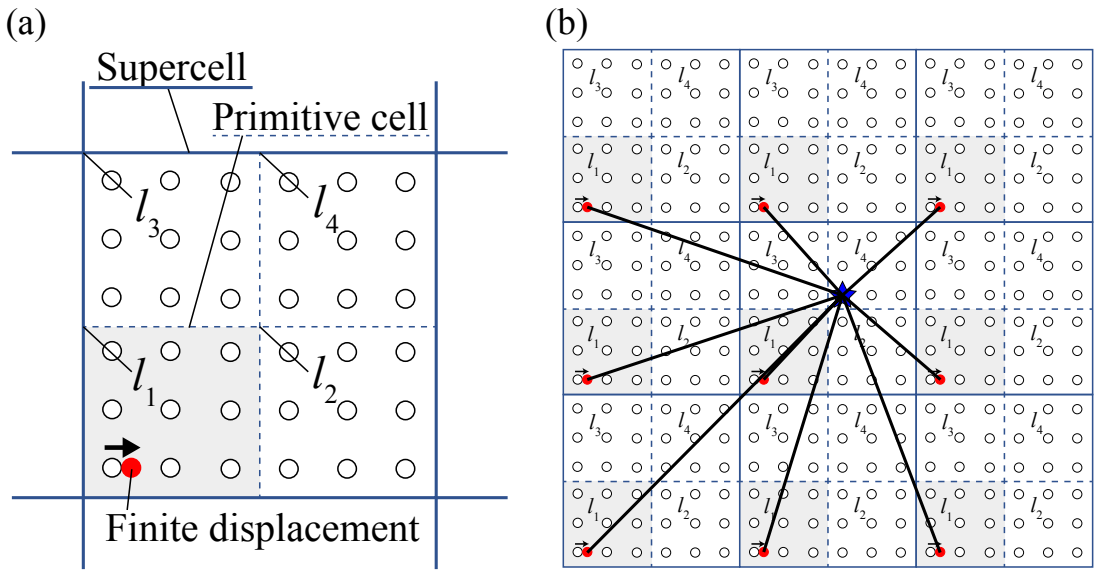

Fig. 5. (Color online) (a) A supercell contains $|\mathrm{P}_{\mathrm{p}\to\mathrm{s}}|$ primitive cells, where atoms are depicted by circles. A finite displacement is introduced in one of the primitive cells. l_1, l_2, l_3, and l_4 are the indices of the lattice points (or primitive cells) in the supercell. The displacement in the supercell breaks the periodicity inside the supercell. (b) Forces in the supercell are calculated under the periodic boundary condition of the supercell. The atom near the center of the figure (filled star symbol) feels the displacements in all mirror images of the supercell.

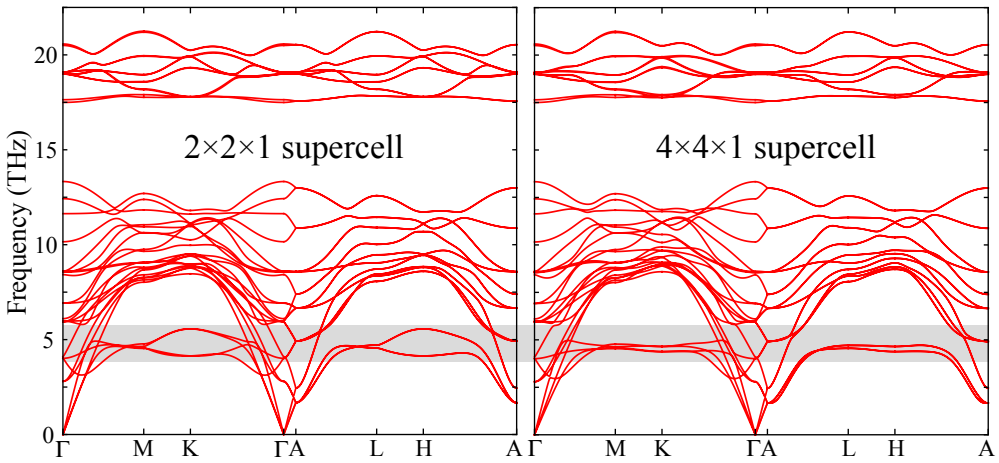

Fig. 6. (Color online) Phonon band structures of Ti_3SiC_2 calculated using $2 \times 2 \times 1$ (left) and $4 \times 4 \times 1$ (right) supercells. Clear difference is observed in the shaded frequency range around 5 THz.

The dynamical matrix in Eq. (9) is approximately constructed by summing over the lattice points inside the supercell [l_1 to l_4 in Fig. 5(a)] instead of the lattice points in the whole crystal. To preserve symmetry of the dynamical matrix, as a normal choice, the phase factor $e^{i\mathbf{q}\cdot(\mathbf{R}^0_{l'\kappa'}-\mathbf{R}^0_{0\kappa})}$ is calculated as the average over the phase factors of those shortest pairs by $|\mathbf{R}^0_{l'\kappa'} - \mathbf{R}^0_{0\kappa}|$ in the supercell periodicity when equidistant shortest pairs exist.[17] The dynamical matrices of the supercell force constants calculated in this way are exact only at the wave vectors commensurate with the supercell dimension $P_{p\to s}$. At the other wave vectors, they are calculated as the results of the Fourier interpolations. Since atomic interactions are expected to decay with increasing distances among atoms, if a sufficiently large supercell is used, the interpolated dynamical matrix becomes a good approximation.

An example of the effect of the supercell size is shown in Fig. 6. These phonon band structures of Ti_3SiC_2 were calculated for this review using $2 \times 2 \times 1$ and $4 \times 4 \times 1$ supercells. The computational details are similar to those found in Ref. 59, however, the generalized gradient approximation of Perdew, Burke, and Ernzerhof revised for solids (PBEsol)[60] was employed as the exchange correlation potential. These phonon band structures are almost identical except for the bands in the frequency range around 5 THz where the phonons are localized. These phonons are attributed mainly to vibrations of Si atoms[59] (see Fig. 8). This means that the interactions between Si atoms are considered relatively long range compared with the other atomic interactions in Ti_3SiC_2. The $4 \times 4 \times 1$ supercell should be used to describe the fine phonon band structure. However, since most of phonon frequencies are well converged at the $2 \times 2 \times 1$ supercell, use of the smaller supercell may be acceptable depending on the purpose of the calculation, e.g., for phonon thermal properties.

3.5 Non-analytical term correction

Atomic displacements in crystal induce electrostatic polarization in ionic crystals. Atomic interaction by the polarization is by far longer-range than the supercell size accessible by practical first-principles calculation. Therefore, this is treated differently from the supercell force constants

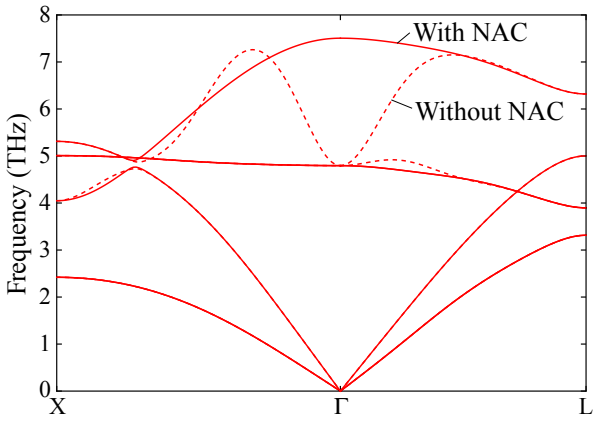

Fig. 7. (Color online) Phonon band structures of NaCl with (solid curves) and without (dashed curves) NAC.

calculation of Eq. (18). An approach that the phonopy code employs is so-called non-analytical term correction (NAC).[13,15,61,62] Dipole–dipole interaction is calculated from static dielectric constant tensor and Born effective charges that are obtained by a DFPT calculation.[13,15,62] This contribution is included to the dynamical matrix of Eq. (9) at each wave vector. To apply this approach to the supercell force constants, a part of the dipole–dipole interaction included at the supercell force constants calculation of Eq. (18) is subtracted from the supercell force constants to avoid double counting the contribution. Then the long-range interactions are added to the dynamical matrix at each wave vector. More details about the NAC implementation in the phonopy code will be written elsewhere.

An example of application of NAC to NaCl is shown in Fig. 7. This calculation was performed using the raw data of the harmonic phonon calculation used in Ref. 63. The difference between the phonon frequencies calculated with and without NAC becomes larger approaching to the Γ point and the effect of NAC tends to be larger for higher frequency modes. Whether the use of NAC is necessary or not depends on research purposes. In many crystals, harmonic thermal properties may be well predicted without NAC.

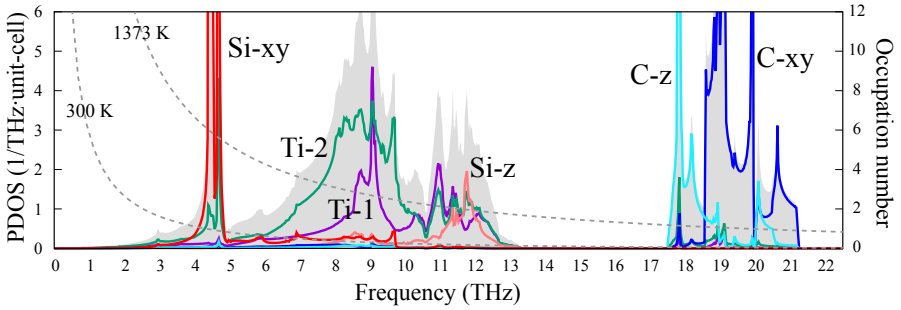

Fig. 8. (Color online) Phonon DOS (shaded) and PDOS (solid curves) of Ti_3SiC_2. The crystal structure of Ti_3SiC_2 is shown in Fig. 9. Si-xy and C-xy mean the DOS projected onto the vibrations of these atoms parallel to the basal plane and Si-z and C-z are those perpendicular to the basal plane. Ti-1 and Ti-2 are plotted independently by their different Wyckoff positions. Dashed curves depict harmonic phonon occupation number [Eq. (16)] at 300 and 1373 K.

3.6 *Density of states*

Phonon density of states (DOS) per unit cell is written as[64]

$$D(\omega) = \frac{1}{N}\sum_{\mathbf{q}\nu}\delta(\omega-\omega_{\mathbf{q}\nu}) \sim \frac{V_c}{(2\pi)^3}\int d\mathbf{q}\sum_{\nu}\delta(\omega-\omega_{\mathbf{q}\nu}). \tag{20}$$

This calculation is a Brillouin zone (BZ) integration. In the numerical calculation of the BZ integration, normally reciprocal primitive cell is discretized using a regular grid of $\mathbf{q}$. In smearing methods, the delta function is replaced by a reasonable bell-shaped function whose integral is one, e.g., Gaussian or Lorentzian function shapes. Another popular BZ integration methods are tetrahedron methods. In the phonopy code, a linear tetrahedron method based on the algorithms of Refs. 65 and 66 is implemented.

Since phonon eigenvector $W_{\kappa\alpha}(\mathbf{q}\nu)$ tells how each atom vibrates in the phonon mode $\mathbf{q}\nu$ [see Eq. (13)], to represent particular atomic contributions to DOS, Eq. (20) is projected onto the norms of the eigenvector elements as

$$D_{\kappa\alpha}(\omega) = \frac{1}{N}\sum_{\mathbf{q}\nu}\delta(\omega-\omega_{\mathbf{q}\nu})|W_{\kappa\alpha}(\mathbf{q}\nu)|^2. \tag{21}$$

$D_{\kappa\alpha}(\omega)$ is a projected DOS (PDOS). Note that $\sum_{\kappa\alpha}D_{\kappa\alpha}(\omega) = D(\omega)$ because of Eq. (12), i.e., orthonormality of eigenvectors.[50] Another convenient PDOS is defined by $D_{\kappa}(\omega) = \sum_{\alpha}D_{\kappa\alpha}(\omega)$.

As an example, phonon DOS and PDOS of Ti_3SiC_2 calculated using the $4\times4\times1$ supercell are shown in Fig. 8. We can see that the localized phonons around 5 THz are mostly attributed to vibrations of Si atoms parallel to the basal plane. Vibration of Si atoms perpendicular to the basal plane is located at much higher frequencies. Direction dependence of vibrations can be seen in C atoms, too. For Ti atoms, the projections onto directions were not shown, since they were found relatively isotropic.

3.7 *Atomic displacements at finite temperatures*

Mean-squared displacements of atoms at finite temperatures within the harmonic approximation are derived from Eqs. (13) and (14) using the commutation relations of phonon creation and annihilation operators as

$$\langle|u_{l\kappa\alpha}|^2\rangle = \frac{1}{Nm_\kappa}\sum_{\mathbf{q}\nu}\frac{\hbar}{2\omega_{\mathbf{q}\nu}}[1+2n_{\mathbf{q}\nu}(T)]|W_{\kappa\alpha}(\mathbf{q}\nu)|^2. \tag{22}$$

Equation (22) can be seen as a weighted PDOS integrated over phonon frequency. The numerical calculation is performed by a simple summation over phonon modes on the regular grid of $\mathbf{q}$. Applications of this calculation are found, e.g., in Refs. 67 and 68. Using sophisticated visualization software for crystals such as VESTA[69] or CrystalMaker,[70] the mean-squared displacements are visualized nicely as thermal ellipsoids. As an example, its visualization of Ti_3SiC_2 calculated at 1373 K is shown in Fig. 9. Si atoms show strongly anisotropic mean-squared displacements. This is explained by the characteristic phonon PDOS as shown in Fig. 8, where PDOS of Si atoms vibrating parallel (Si-xy) and perpendicular (Si-z) to the basal plane accommodate in well-separated frequency regions. Since low frequency modes have larger contribution by $1/\omega_{\mathbf{q}\nu}$ and $n_{\mathbf{q}\nu}$ in Eq. (22), the mean-squared displacements of Si atoms are calculated as elongated in x–y direction. Those of C atoms show ellipsoids elongated slightly in z direction as can be guessed from PDOS in Fig. 8. Neutron diffraction measurement by Lane et al. presented a good agreement in the mean-squared displacements between the experiment and calculation of Ti_3SiC_2.[67]

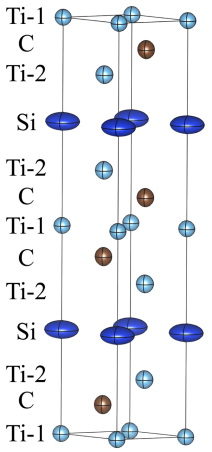

Fig. 9. (Color online) Unit cell of Ti_3SiC_2 ($P6_3/mmc$) drawn using VESTA software.[69] Atoms are drawn as 99% probability thermal ellipsoids calculated at 1373 K.

The mean-squared displacement projected onto a unit vector $\hat{\mathbf{n}}$ may be useful being defined as

$$\langle|\hat{\mathbf{n}}\cdot\mathbf{u}_{l\kappa}|^2\rangle = \frac{1}{Nm_\kappa}\sum_{\mathbf{q}\nu}\frac{\hbar}{2\omega_{\mathbf{q}\nu}}[1+2n_{\mathbf{q}\nu}(T)]|\hat{\mathbf{n}}\cdot\mathbf{W}_{\kappa}(\mathbf{q}\nu)|^2. \tag{23}$$

This is used for the calculation of harmonic Debye–Waller factor $e^{-\frac{1}{2}\langle|\mathbf{Q}\cdot\mathbf{u}_\kappa|^2\rangle}$ in one-phonon dynamic structure factor [Eq. (26)] in the phonopy code.

3.8 *Dynamic structure factor*

Phonon spectra at general points are measured by inelastic neutron scattering (INS) and inelastic X-ray scattering (IXS). The INS and IXS measurements require large instruments that are shared by many researchers. Since the beam time for the measurements is limited, it is useful to estimate dynamics structure factor $S(\mathbf{Q},\nu,\omega)$ in advance to choose the best $\mathbf{Q}$ points for the measurements. In the measurement, incident neutrons (INS) or photons (IXS) are scattered by crystal. The wave vector relation is written as $\mathbf{Q}=\mathbf{k}-\mathbf{k}'$, where $\mathbf{k}$ and $\mathbf{k}'$ denote the wave vectors of the incident and scattered particles, respectively. For INS, one-phonon dynamic structure factor under the harmonic approximation is given as[71,72]

$$S(\mathbf{Q},\nu,\omega)^{+1\mathrm{ph}} = \frac{k'}{k}\frac{N}{\hbar}\sum_{\mathbf{q}}|F(\mathbf{Q},-\mathbf{q}\nu)|^2(n_{\mathbf{q}\nu}+1)\delta(\omega-\omega_{\mathbf{q}\nu})\Delta(\mathbf{Q}-\mathbf{q}), \tag{24}$$

$$S(\mathbf{Q},\nu,\omega)^{-1\mathrm{ph}} = \frac{k'}{k}\frac{N}{\hbar}\sum_{\mathbf{q}}|F(\mathbf{Q},\mathbf{q}\nu)|^2 n_{\mathbf{q}\nu}\delta(\omega+\omega_{\mathbf{q}\nu})\Delta(\mathbf{Q}+\mathbf{q}), \tag{25}$$

with

$$F(\mathbf{Q},\mathbf{q}\nu) = \sum_\kappa\sqrt{\frac{\hbar}{2m_\kappa\omega_{\mathbf{q}\nu}}}\bar{b}_\kappa e^{-\frac{1}{2}\langle|\mathbf{Q}\cdot\mathbf{u}_\kappa|^2\rangle}e^{i(\mathbf{Q}+\mathbf{q})\cdot\mathbf{R}^0_{0\kappa}}\mathbf{Q}\cdot\mathbf{W}_\kappa(\mathbf{q}\nu), \tag{26}$$

where $\bar{b}_\kappa$ is the average scattering length, and $\Delta(\mathbf{Q}\pm\mathbf{q})\equiv 1$ when the wave vector $\mathbf{Q}\pm\mathbf{q}$ is any reciprocal lattice vector $\mathbf{G}$, otherwise 0. Note that the phase factor of the last equation is different from that in Ref. 71 because Ref. 71 employs dynamical matrix of Eq. (10). One phonon is created in Eq. (24) and absorbed in Eq. (25).

The dynamic structure factor is not a periodic function of $\mathbf{G}$. Intensity of the phonon measurement depends largely on the choice of BZ (or $\mathbf{G}$) that $\mathbf{Q}$ belongs as it is clear from the factor $\mathbf{Q}\cdot\mathbf{W}_\kappa(\mathbf{q}\nu)$ in $F(\mathbf{Q},\mathbf{q}\nu)$. The inner product $\mathbf{Q}\cdot\mathbf{W}_\kappa(\mathbf{q}\nu)$ shows that Eq. (24) is sensitive to the polarization (eigenvector) of atoms in each phonon mode. In general, it is difficult to guess $\mathbf{W}_\kappa(\mathbf{q}\nu)$ for a variety of crystals either quantitatively or qualitatively. Therefore, the first-principles phonon calculation became an indispensable tool for the experimental phonon measurements.

As an example, the phonon calculation of the dynamic structure factor was performed for NaCl using the atomic form factor $f_\kappa(\mathbf{Q})$ data of Na^+ and Cl^- from Ref. 73 instead of $\bar{b}_\kappa$, where the computational details are similar to those used for Fig. 7. Figure 10 shows the IXS spectra of NaCl at 300 K at the wave vector $\mathbf{Q}=(3.23\ 3.23\ 3.23)$ from Ref. 74 and the calculated $S(\mathbf{Q},\nu,\omega)^{+1\mathrm{ph}}$. Although the phonon frequencies slightly underestimate the peak positions of the IXS spectra, we can see that the dynamic structure factor calculation estimates well the IXS peak intensities.

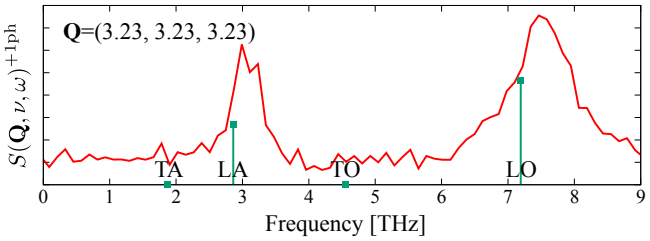

Fig. 10. (Color online) The solid curve shows the IXS spectra of NaCl at 300 K at the wave vector $\mathbf{Q}=(3.23\ 3.23\ 3.23)$ measured in the study of Ref. 74. The lengths of the vertical lines depict calculated $S(\mathbf{Q},\nu,\omega)^{+1\mathrm{ph}}$.

3.9 *Thermal properties at constant volume*

Under the harmonic approximation, the phonon partition function has the simple form:

$$Z_{\mathrm{ha}} = \prod_{\mathbf{q}\nu}\frac{e^{-\hbar\omega_{\mathbf{q}\nu}/2k_\mathrm{B}T}}{1-e^{-\hbar\omega_{\mathbf{q}\nu}/k_\mathrm{B}T}}. \tag{27}$$

From Z_{ha}, Helmholtz free energy F_{ha} and entropy S_{ha} are obtained as

$$F_{\mathrm{ha}} = \frac{1}{2}\sum_{\mathbf{q}\nu}\hbar\omega_{\mathbf{q}\nu} + k_\mathrm{B}T\sum_{\mathbf{q}\nu}\ln[1-e^{-\hbar\omega_{\mathbf{q}\nu}/k_\mathrm{B}T}], \tag{28}$$

$$S_{\mathrm{ha}} = \frac{1}{2T}\sum_{\mathbf{q}\nu}\hbar\omega_{\mathbf{q}\nu}\coth(\hbar\omega_{\mathbf{q}\nu}/2k_\mathrm{B}T) - k_\mathrm{B}\sum_{\mathbf{q}\nu}\ln[2\sinh(\hbar\omega_{\mathbf{q}\nu}/2k_\mathrm{B}T)]. \tag{29}$$

Heat capacity at constant volume $C_{V,\mathrm{ha}}$ is calculated from Eq. (17) as

$$C_{V,\mathrm{ha}} = \sum_{\mathbf{q}\nu}k_\mathrm{B}\left(\frac{\hbar\omega_{\mathbf{q}\nu}}{k_\mathrm{B}T}\right)^2\frac{\exp(\hbar\omega_{\mathbf{q}\nu}/k_\mathrm{B}T)}{[\exp(\hbar\omega_{\mathbf{q}\nu}/k_\mathrm{B}T)-1]^2}. \tag{30}$$

Numerical calculations of these thermal properties are performed by simple summations over phonon modes sampled on a regular grid of $\mathbf{q}$ similar to Eq. (22).

As an example, thermal properties of Al is presented in Fig. 11. The experimental heat capacity[75] is also shown in Fig. 11 to compare with the calculated values. At low temperatures, the experimental value and the calculated $C_{V,\mathrm{ha}}$ tend to agree well. Increasing temperature, $C_{V,\mathrm{ha}}$ deviates from the experimental value since effect of thermal expansion is ignored. Using QHA, heat capacity at constant pressure (C_P) is calculated as presented in Sect. 4.2, and the agreement with the experiment becomes better. In this Al example, only phonon contribution to the thermal properties was considered. For metals, entropic contribution from electron can be non-negligible depending on electronic structures. Other contributions by atomic configurations in alloys, quasiparticles such as magnons, etc., would have to be considered for research purposes. However, phonon is a major source of these thermal properties.

3.10 *Phonon group velocity*

Calculation of phonon group velocity is useful in estimating LTC (see Sect. 6). When a phonon wave packet is well defined in crystal, it travels with the phonon group velocity.[32] The phonon group velocity $\mathbf{v}_{\mathbf{q}\nu}$ is written as

$$v_{\mathbf{q}\nu,\alpha} \equiv \frac{\partial\omega_{\mathbf{q}\nu}}{\partial q_\alpha}$$

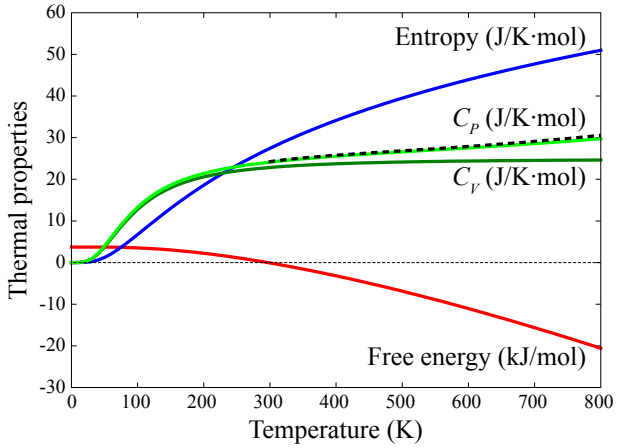

Fig. 11. (Color online) Phonon thermal properties of Al from Ref. 26 licensed under CC-BY-4.0. The solid curves show the calculated thermal properties of Helmholtz free energy ($F_{\rm ha}$), entropy ($S_{\rm ha}$), heat capacity at constant volume ($C_{V,{\rm ha}}$), and heat capacity at constant pressure (C_P) by quasi-harmonic approximation. The dashed curve depicts the experimental value of the heat capacity from the NIST-JANAF thermochemical tables.[75]

$$= \frac{1}{2\omega_{\mathbf{q}\nu}} \frac{\partial \omega^2_{\mathbf{q}\nu}}{\partial q_\alpha}$$
$$= \frac{1}{2\omega_{\mathbf{q}\nu}} \sum_{\kappa\beta,\kappa'\beta'} W^*_{\kappa\beta}(\mathbf{q}\nu) \frac{\partial D_{\kappa\beta,\kappa'\beta'}(\mathbf{q})}{\partial q_\alpha} W_{\kappa'\beta'}(\mathbf{q}\nu). \quad (31)$$

The last equality is easier to handle than the first equality in the numerical phonon calculation, since treatment of phonon-mode connectivity in the phonon band structure is avoided. The derivative of the dynamical matrix with respect to $\mathbf{q}$ in the last equality of Eq. (31) is performed analytically or numerically. The analytical derivative is easily done for Eq. (9). However, when using NAC, the phonopy code employs a finite difference method, i.e.,

$$\frac{D_{\kappa\beta,\kappa'\beta'}(\mathbf{q} + \Delta\mathbf{q}_\alpha) - D_{\kappa\beta,\kappa'\beta'}(\mathbf{q} - \Delta\mathbf{q}_\alpha)}{2|\Delta\mathbf{q}_\alpha|}, \quad (32)$$

since the approximation (32) is numerically stable, accurate enough, and implemented straightforwardly.

3.11 Irreducible representation

Each phonon mode belongs to one of irreducible representations of the space group at $\mathbf{q}$. It is easy to compute the irreducible representation from the calculated phonon eigenvectors.

A space group operation $\mathrm{S} = \{\mathrm{R}|\tau\}$, where R and τ are the rotation and translation parts, respectively, is applied to the eigenvector as follows:[53]

$$\mathbf{W}_{\kappa'}(\mathbf{q}\nu) = \sum_{\kappa} \mathrm{R}\mathbf{W}_\kappa(\mathbf{q}\nu) e^{i\mathbf{q}\cdot(\mathrm{S}^{-1}\mathbf{R}_{0\kappa'} - \mathbf{R}_{0\kappa'})} \delta_{\mathrm{S}\kappa,\kappa'}. \quad (33)$$

$\delta_{\mathrm{S}\kappa,\kappa'}$ in Eq. (33) means that κ is sent to κ' by $\mathrm{S} = \{\mathrm{R}|\tau\}$. For a little group operation $\mathrm{S}_\mathbf{q} = \{\mathrm{R}_\mathbf{q}|\tau_\mathbf{q}\}$, $\mathbf{q} = \mathrm{R}_\mathbf{q}\mathbf{q} + \mathbf{G}$, the element of the irreducible representation is calculated by

$$\Gamma_{\nu\nu'}(\mathrm{S}_\mathbf{q}) = \sum_{\kappa\kappa'} \mathbf{W}^*_{\kappa'}(\mathbf{q}\nu) \mathrm{R}_\mathbf{q} \mathbf{W}_\kappa(\mathbf{q}\nu') \times e^{i\mathbf{q}\cdot(\mathrm{S}_\mathbf{q}^{-1}\mathbf{R}_{0\kappa'} - \mathbf{R}_{0\kappa'})} \delta_{\mathrm{S}_\mathbf{q}\kappa,\kappa'}. \quad (34)$$

By Eq. (34), the irreducible representation $\Gamma_{\nu\nu'}$ whose dimension is larger than one is obtained as one of equivalent representations, i.e., it may not be numerically unique. The characters (traces of irreducible representation elements) are determined uniquely. Reliable character tables of space-group types are found at the bilbao crystallographic server.[76] Comparing calculated characters and the reference character tables, phonon modes are assigned to the symbols of the irreducible representations.

4. Quasi-harmonic Phonon Calculation

Phonon frequency changes under applied strain. This is an anharmonic effect, but sometimes called quasi harmonicity although this word can mean different phenomena in different contexts.[51] In the following sections, examples where QHA is applied are presented.

4.1 Mode Grüneisen parameter

In Fig. 12(a), phonon DOS of Al calculated at different unit-cell volumes are presented. These DOS were calculated using the computational details as written in Ref. 26. Phonon frequencies of many crystals tend to increase by compressing unit cell. As shown in Fig. 12(b), roughly-linear relation of phonon frequency with respect to a wide range of unit cell volume is observed. This linear trend (either positive or negative) is a typical behavior. As a measure of quasi anharmonicity of crystals, the linear coefficient is defined as mode Grüneisen-parameter,

$$\gamma_{\mathbf{q}\nu} = -\frac{V_{\rm c}}{\omega_{\mathbf{q}\nu}} \frac{\partial \omega_{\mathbf{q}\nu}}{\partial V_{\rm c}}. \quad (35)$$

This is computed from the derivative of dynamical matrix similarly to Eq. (31) but with respect to unit cell volume by

$$\gamma_{\mathbf{q}\nu} = -\frac{V_{\rm c}}{2\omega^2_{\mathbf{q}\nu}} \sum_{\kappa\alpha,\kappa'\alpha'} W^*_{\kappa\alpha}(\mathbf{q}\nu) \frac{\partial D_{\kappa\alpha,\kappa'\alpha'}(\mathbf{q}, V_{\rm c})}{\partial V_{\rm c}} W_{\kappa'\alpha'}(\mathbf{q}\nu). \quad (36)$$

In the numerical calculation, finite difference method similar to the approximation (32) is used in the implementation of the phonopy code. The mode Güneisen parameter distribution of Al sampled on a regular grid of $\mathbf{q}$ is shown in Fig. 12(c).

4.2 Thermal expansion

Due to the quasi anharmonicity, the Helmholtz free-energy in Eq. (28) is dependent on unit-cell volume and temperature, i.e., $F_{\rm ha}(V_{\rm c}; T)$. If we approximate the Helmholtz free-energy as $U_{\rm el}(V_{\rm c}) + F_{\rm ha}(V_{\rm c}; T)$, where $U_{\rm el}(V_{\rm c})$ is the electronic total energy that can be also obtained from the first-principles calculation, we can draw this energy function with respect to $V_{\rm c}$ and T as shown in Fig. 13(a). Gibbs free-energy is given by the following thermodynamic relation:

$$G(T, p) = \min_{V_{\rm c}} [U_{\rm el}(V_{\rm c}) + F_{\rm ha}(V_{\rm c}; T) + pV_{\rm c}], \quad (37)$$

where p denotes the pressure. In the practical QHA calculation, the energy functions are calculated at sampling points of unit cell volumes as shown in Fig. 13(a), and the energies are fitted to a nice smooth function such as equation of states.[77] At $p = 0$, the energy bottom corresponds to the Gibbs free energy. In Fig. 13(a), the cross symbols indicate the Gibbs free-energies at temperatures. The equilibrium unit cell volume at (T, p) is obtained likewise by

$$V^{\rm eq}_{\rm c}(T, p) = \arg\min_{V_{\rm c}} [U_{\rm el}(V_{\rm c}) + F_{\rm ha}(V_{\rm c}; T) + pV_{\rm c}]. \quad (38)$$

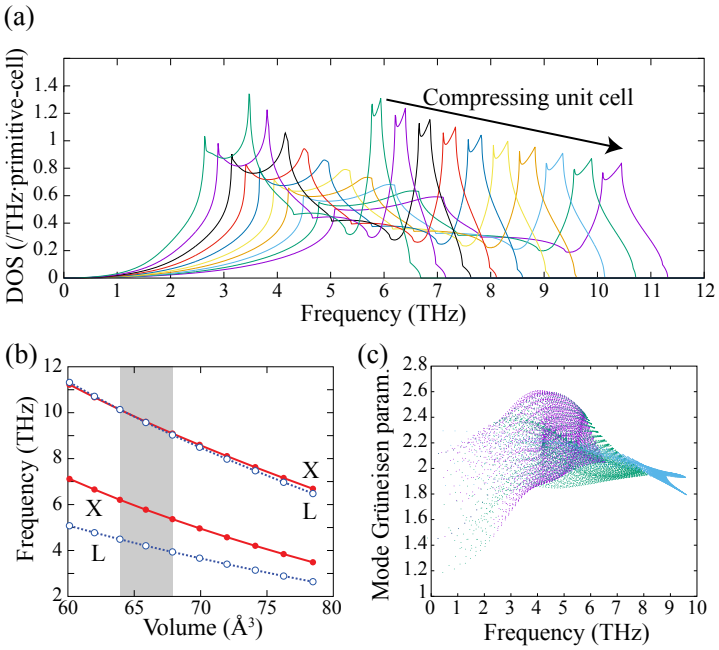

Fig. 12. (Color online) (a) Calculated phonon DOS of Al at different unit cell volumes. Compressing unit cell shifts phonon DOS to higher frequency. The volume points used for the phonon DOS calculations are same as those in (b). (b) Calculated phonon frequencies of Al at X (filled circle symbols) and L (open circle symbols) points at different unit cell volumes. This figure is obtained from Ref. 26 licensed under CC-BY-4.0. (c) Calculated mode Grüneisen parameters of Al. The reciprocal primitive cell was sampled by the $64 \times 64 \times 64$ mesh. Equation (36) was computed using the finite difference method with respect to unit cell volume. The volume difference ΔV_c used for the calculation is presented as shaded area in (b). Different colors of the points show the different phonon band indices ordered by phonon frequencies at respective **q**-points.

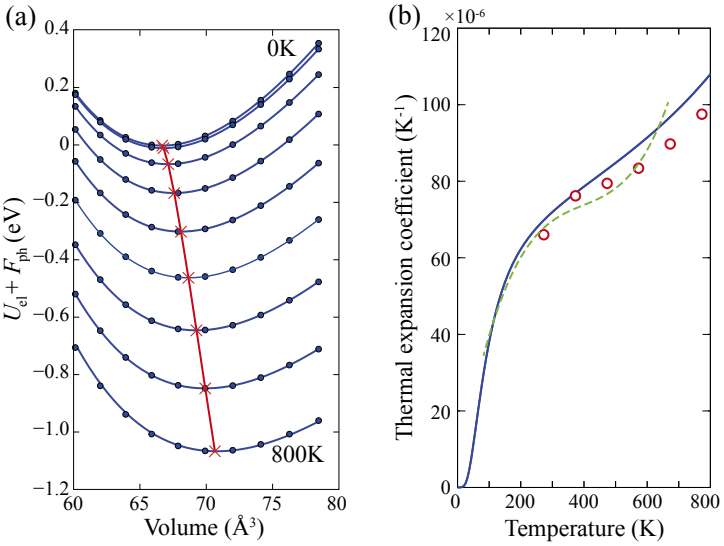

Fig. 13. (Color online) These figures are obtained from Ref. 26 licensed under CC-BY-4.0. (a) Calculated values of $U_{el}(V_c) + F_{ha}(V_c; T)$ of Al with respect to unit cell volumes at temperatures. $U_{el}(V_c) + F_{ha}(V_c; T)$ at each temperature (filled circle symbols) was fitted to the Vinet equation of states[77] (solid curves). Bottoms of the energy curves correspond to Gibbs free energies at the temperatures at $p = 0$ that are marked by cross symbols. Equilibrium volumes are obtained simultaneously. (b) Solid curve depicts calculated volumetric thermal expansion coefficients of Al at temperatures. Circle symbols[78] and dashed curve[79] are the experimental values.

From the equilibrium volumes at temperatures, thermal expansion coefficients are calculated as shown in Fig. 13(b). A good agreement with the experimental values is obtained for Al.

In Fig. 11, the heat capacity at constant pressure (C_P) of Al is presented. This was calculated by the thermodynamic relation:

$$C_P(T,p) = -T\frac{\partial^2 G(T,p)}{\partial T^2}$$

$$= C_{V,\mathrm{ha}}[T; V_c(T,p)] + T\frac{\partial V_c(T,p)}{\partial T}\frac{\partial S_{\mathrm{ha}}(T; V_c)}{\partial V_c}\bigg|_{V_c = V_c(T,p)}. \quad (39)$$

The second equation is more stable numerically.

4.3 Structural phase transition under shear strain

The quasi harmonicity also appears under applied shear strain. Hexagonal-close-packed (HCP) Ti is known to exhibit twinning deformation.[80] The $\{10\bar{1}2\}$ twinning mode that

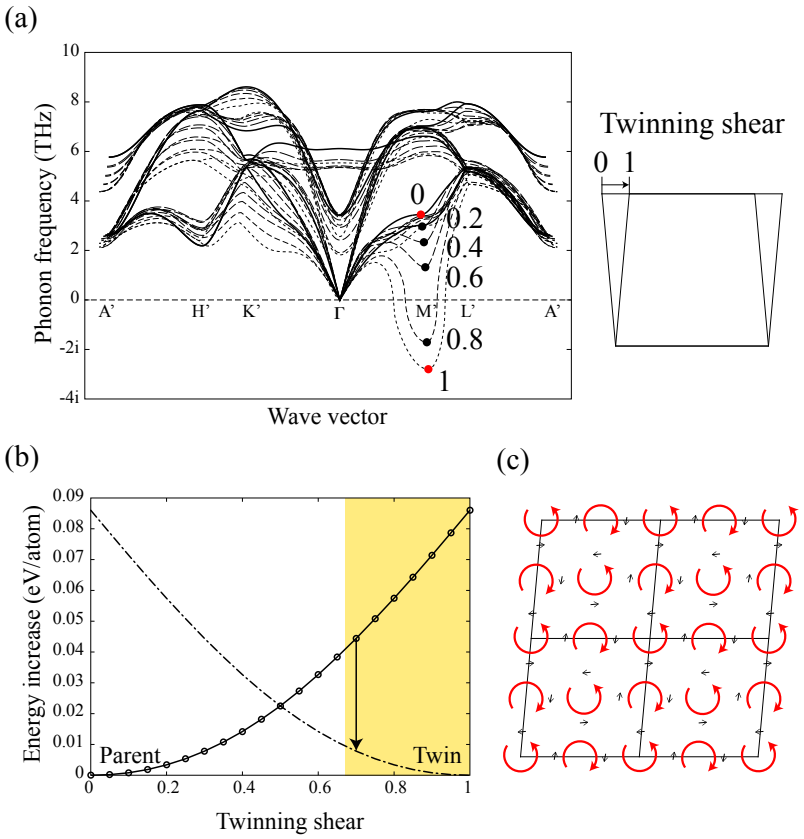

Fig. 14. (Color online) These figures are obtained from Ref. 81 licensed under CC-BY-4.0. (a) Phonon band structure change of HCP Ti under applying shear deformation of $\{10\bar{1}2\}$ twinning mode. Filled-circle symbols depict phonon frequencies of characteristic phonon mode. The values next to the symbols indicate amount of twinning shear, where 0 (parent) means the original HCP shape and 1 (twin) means another HCP lattice having different orientation from the original HCP lattice. The HCP lattices at the parent and twin are displayed next to the phonon band structure. Above ∼0.7 twinning-shear, crystal structure becomes dynamically unstable and spontaneous structural transformation occurs. (b) Electronic total energy of shear strained Ti with respect to the twinning shear. Applying the twinning shear, the energy increases monotonically. Symmetry breaking due to the spontaneous structure transformation relaxes the crystal structure to the twin, i.e., the HCP Ti having different orientation (twin) with respect to the original HCP Ti (parent). The vertical arrow shows the energy released by the relaxation at the fixed twinning shear. (c) Rearrangement of atomic positions by the spontaneous structural transformation. Small arrows depict the atomic displacements. Circular arrows illustrate the collective atomic displacements introduced by the transformation, which is related to shuffling mechanism of the $\{10\bar{1}2\}$ twinning mode.

corresponds to a specific shear strain is observed most frequently among the different twinning modes in Ti. In Ref. 81, phonon structure change under the applied specific strain was studied, and a characteristic phonon mode was found particularly sensitive to this twinning deformation. As shown in Fig. 14(a), phonon frequency of the characteristic phonon mode indicated by filled circles drastically changes applying small shear-strain, and eventually the crystal structure exhibits spontaneous structural transformation at ∼0.7 twinning shear where the phonon frequency becomes imaginary. The measure of the twinning shear is shown next to Fig. 14(a), where the shape of the lattice is transformed from the hexagonal lattice to the extended lattice that conveniently represents the $\{10\bar{1}2\}$ twinning mode by an integer transformation matrix similarly to Eq. (19).[81] The spontaneous transition releases stored elastic energy [Fig. 14(b)], and the original HCP Ti (parent) transforms to the HCP Ti having different orientation (twin) by rearranging atomic positions that are displayed by small arrows in Fig. 14(c).

At the twinning shear where the characteristic phonon mode exhibits imaginary frequency, symmetry of the crystal structure model was broken introducing tiny atomic displacements corresponding to Eq. (13) of the characteristic phonon mode with a small value of $Q(\mathbf{q}\nu)$. The crystal structure with the broken symmetry was relaxed by the first-principles calculation to observe rearrangements of atomic positions. Movements of atoms during the relaxation can be tracked since the atoms are labeled. The collective displacements indicated by circular arrows in Fig. 14 are recognized as a shuffling mechanism of the $\{10\bar{1}2\}$ twinning mode.

The phonon calculations at the different twinning shears in this study[81] were performed systematically using an automated phonon calculation workflow presented in Sect. 7. Once the calculation workflow is automated, this research approach is easily applicable to the other twinning modes. It would be also used to discover unknown twinning modes of crystals.

5. Anharmonic Phonon Calculation

In this and following sections, composite indices $\mathbf{q}\nu$ and $-\mathbf{q}\nu$ are abbreviated by λ and $-\lambda$, respectively.

5.1 Phonon coordinate transformation

Anharmonic terms of Eq. (1) may be expanded with respect to phonon operators $(a_\lambda + a^\dagger_{-\lambda})$ instead of atomic displacements. Then, the third-order terms in Eq. (1) are written as

$$\mathscr{H}_3 = \sum_{\lambda\lambda'\lambda''} \Phi_{\lambda\lambda'\lambda''}(a_\lambda + a^\dagger_{-\lambda})(a_{\lambda'} + a^\dagger_{-\lambda'})(a_{\lambda''} + a^\dagger_{-\lambda''}). \quad (40)$$

$\Phi_{\lambda\lambda'\lambda''}$ is obtained by substituting Eqs. (13) and (14) into the third-order terms of Eq. (1) as[50]

$$\begin{aligned}\Phi_{\lambda\lambda'\lambda''} = {} & \frac{1}{\sqrt{N}}\frac{1}{3!}\sum_{\kappa\kappa'\kappa''}\sum_{\alpha\alpha'\alpha''} W_{\lambda,\kappa\alpha}W_{\lambda',\kappa'\alpha'}W_{\lambda'',\kappa''\alpha''} \\ & \times \sqrt{\frac{\hbar}{2m_\kappa\omega_\lambda}}\sqrt{\frac{\hbar}{2m_{\kappa'}\omega_{\lambda'}}}\sqrt{\frac{\hbar}{2m_{\kappa''}\omega_{\lambda''}}} \\ & \times \sum_{l'l''} \Phi_{0\kappa\alpha,l'\kappa'\alpha',l''\kappa''\alpha''} e^{i\mathbf{q}'\cdot(\mathbf{R}^0_{l'\kappa'}-\mathbf{R}^0_{0\kappa})} e^{i\mathbf{q}''\cdot(\mathbf{R}^0_{l''\kappa''}-\mathbf{R}^0_{0\kappa})} \\ & \times e^{i(\mathbf{q}+\mathbf{q}'+\mathbf{q}'')\cdot\mathbf{R}^0_{0\kappa}}\Delta(\mathbf{q}+\mathbf{q}'+\mathbf{q}''). \end{aligned} \quad (41)$$

$\Delta(\mathbf{q}+\mathbf{q}'+\mathbf{q}'')$ in Eq. (41) is the same as that defined for Eq. (24), which is the result of translational symmetry of force constants:

$$\Phi_{l\kappa\alpha,l'\kappa'\alpha',l''\kappa''\alpha''} = \Phi_{0\kappa\alpha,(l'-l)\kappa'\alpha',(l''-l)\kappa''\alpha''}. \quad (42)$$

Higher order terms are transformed similarly, but only the third-order terms are treated as anharmonic terms in this review.

We can calculate all the values in Eq. (41) from the harmonic phonon calculation except for the third-order force constants $\Phi_{l\kappa\alpha,l'\kappa'\alpha',l''\kappa''\alpha''}$. In the phono3py code, the third-order supercell force constants are calculated in a similar approach as Eq. (18) for the harmonic supercell force constants, but the following simultaneous equations are solved:

$$-f_{l\kappa\alpha} = \sum_{l'\kappa'\alpha',l''\kappa''\alpha''} \Phi_{l\kappa\alpha,l'\kappa'\alpha',l''\kappa''\alpha''} u_{l'\kappa'\alpha'} u_{l''\kappa''\alpha''}. \quad (43)$$

In Fig. 5, at least one atom is displaced in the supercell. For the third-order supercell force constants, at least two atoms are displaced in the supercell.[82] As the result, the required number of the supercells containing various configurations of displacements to solve Eq. (43) becomes far larger than that for the harmonic supercell force constants. Normally, the computation is a few orders of magnitude more demanding than that of the harmonic supercell force constants calculation. Often we expect, though not always, that the atomic interaction range in direct space is shorter in higher-order force constants. Assuming this, Eq. (43) can be solved ignoring force-constants elements of atoms whose mutual distances are larger than some cutoff distance. Using this approach, the third-order supercell force constants calculation may become less computationally demanding although sacrificing their numerical accuracy.

The harmonic and anharmonic supercell force constants are also calculated using the specific force constants calculation codes such as the ALM[46] and hiPhive[47] codes. These can perform the supercell force constants calculations applying constrains of a variety of symmetries in addition to the precise control of the cutoff distances. The calculated supercell force constants are directly usable in the phonopy and phono3py codes.

5.2 *Phonon lifetime*

Imaginary part of phonon self energy $\Gamma_\lambda(\omega)$ is computed up to second order in $\mathscr{H}_3$ using many body perturbation theory.[83–85] It takes a form analogous to the Fermi's golden rule,

$$\begin{aligned}\Gamma_\lambda(\omega) = {} & \frac{18\pi}{\hbar^2}\sum_{\lambda'\lambda''}|\Phi_{-\lambda\lambda'\lambda''}|^2\{(n_{\lambda'}+n_{\lambda''}+1) \\ & \times[\delta(\omega-\omega_{\lambda'}-\omega_{\lambda''})-\delta(\omega+\omega_{\lambda'}+\omega_{\lambda''})] \\ & +(n_{\lambda'}-n_{\lambda''})[\delta(\omega+\omega_{\lambda'}-\omega_{\lambda''}) \\ & -\delta(\omega-\omega_{\lambda'}+\omega_{\lambda''})]\}. \end{aligned} \quad (44)$$

The summation over $\mathbf{q}'$ and $\mathbf{q}''$ reduces to the summation over only $\mathbf{q}'$ because $\mathbf{q}'' = \mathbf{G}+\mathbf{q}-\mathbf{q}'$ where the reciprocal lattice vector $\mathbf{G}$ is uniquely determined if the first BZ boundary is defined. Phonon lifetime τ_λ is obtained by setting $\omega = \omega_\lambda$ in Eq. (44) as,[83]

$$\tau_\lambda = \frac{1}{2\Gamma_\lambda(\omega_\lambda)}. \quad (45)$$

The delta function in Eq. (44) eliminates many pairs of λ' and λ'' from the summation in the calculation of $\Gamma_\lambda(\omega_\lambda)$. This allows us to skip non-negligible amount of corresponding computation of $\Phi_{\lambda\lambda'\lambda''}$ in the calculation of phonon lifetime.

In the phono3py code, the BZ integration in Eq. (44), i.e., the summation over λ' and λ'' with the delta functions, is performed either with a smearing method or a linear tetrahedron method similarly to the DOS calculation as explained in 3.6. The former is implemented just by replacing the delta function by the normal distribution function. This method requires one parameter of the smearing width. The latter implementation follows the algorithms of Refs. 65 and 66, which requires no parameter. The former tends to underestimate phonon lifetime compared with the latter. In most cases, it is easier to use the latter method, however, the implementation is more involved. The technical details of the linear tetrahedron method implemented in the phono3py code will be described elsewhere.

5.3 *Phonon spectral function*

Using the phono3py code, phonon spectral function of the bubble diagram in the following form can be calculated,[46,63]

$$A_\lambda(\omega) = \frac{1}{\pi}\frac{4\omega_\lambda^2\Gamma_\lambda(\omega)}{[\omega^2-\omega_\lambda^2-2\omega_\lambda\Delta_\lambda(\omega)]^2+[2\omega_\lambda\Gamma_\lambda(\omega)]^2}, \quad (46)$$

where $\Delta_\lambda(\omega)$ is the real part of the self energy given as[83]

$$\Delta_\lambda(\omega) = \frac{18\pi}{\hbar^2}\sum_{\lambda'\lambda''}|\Phi_{-\lambda\lambda'\lambda''}|^2\left\{\left[\frac{(n_{\lambda'}+n_{\lambda''}+1)}{(\omega-\omega_{\lambda'}-\omega_{\lambda''})_{\mathrm{p}}}-\frac{(n_{\lambda'}+n_{\lambda''}+1)}{(\omega+\omega_{\lambda'}+\omega_{\lambda''})_{\mathrm{p}}}\right]+\left[\frac{(n_{\lambda'}-n_{\lambda''})}{(\omega+\omega_{\lambda'}-\omega_{\lambda''})_{\mathrm{p}}}-\frac{(n_{\lambda'}-n_{\lambda''})}{(\omega-\omega_{\lambda'}+\omega_{\lambda''})_{\mathrm{p}}}\right]\right\}. \quad (47)$$

The symbol p beside the parentheses in the denominators means the Cauchy principal value. $\Delta_\lambda(\omega)$ is calculated by approximating the Cauchy principal value[83] or by employing the Kramers–Kronig relation. To draw the spectral shape of $A_\lambda(\omega)$, Eq. (44) is calculated at the phonon frequencies uniformly sampled in the frequency interval $[0, 2\omega_{\max}]$,

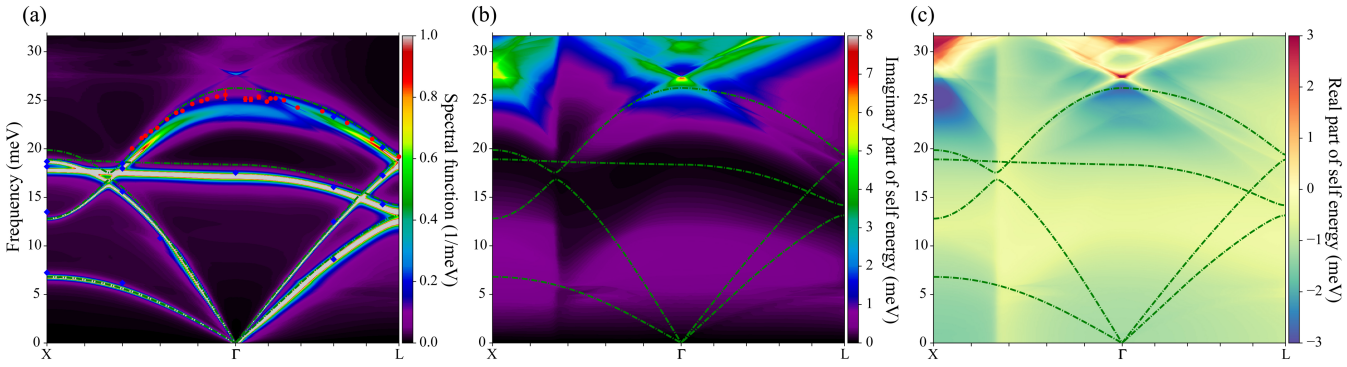

Fig. 15. (Color online) These figures are obtained from Ref. 63 licensed under CC-BY-4.0. From left, (a) spectral function, (b) imaginary part of self energy, and (c) real part of self energy of KCl at 300 K calculated along the X–Γ–L path. The dashed-dotted curves show the renormalized phonon frequencies that correspond to ω_λ. The filled circle and diamond symbols show peak positions of the IXS measurement[63] and the INS measurement by Raunio and Almqvist,[90] respectively. Phonon frequency unit of meV is used in these figures where 1 meV–0.24 THz.

where $\omega_{\max}$ is the highest phonon frequency in BZ. In this case, $\Delta_\lambda(\omega)$ is easily calculated from $\Gamma_\lambda(\omega)$ using the Kramers–Kronig relation since ω for $\Gamma_\lambda(\omega)$ is bounded and $\Gamma_\lambda(\omega)$ itself is calculated using the linear tetrahedron method accurately. To employ the Kramers–Kronig relation, $\Gamma_\lambda(\omega)$ is expanded to $[-2\omega_{\max}, 2\omega_{\max}]$ by using the odd function property of $\Gamma_\lambda(\omega)$.

As an example, phonon spectral function of KCl at 300 K calculated in the study of Ref. 63 is shown in Fig. 15(a). The imaginary and real parts of self energy are shown in Figs. 15(b) and 15(c), respectively. In the study of Ref. 63, the phonon frequency was renormalized by the stochastic self-consistent harmonic approximation (SSCHA),[39,42–44,86–89] and the third-order supercell force constants were calculated under SSCHA. The dashed-dotted curves in Fig. 15 depict the renormalized phonon frequencies that correspond to ω_λ. Due to anharmonicity, the phonon band structure has distribution unlike Fig. 7. In Fig. 15(a), we can see broad longitudinal optical (LO) band in high frequency region. This is attributed mainly to large $\Gamma_\lambda(\omega)$ as shown in Fig. 15(b). Phonon spectral shape may not be approximated well by a Lorentzian function since frequency dependency of $\Gamma_\lambda(\omega)$ and $\Delta_\lambda(\omega)$ [not $\Gamma_\lambda(\omega_\lambda)$ and $\Delta_\lambda(\omega_\lambda)$] creates complicated spectral shape, e.g., the LO band of the spectral function looks disconnected. One of the main reasons of the LO-mode disconnection is that ω_λ curve of the LO-mode passes through the region where $\Delta_\lambda(\omega)$ changes abruptly [near Γ point on the Γ–L path at ∼25 meV in Fig. 15(c)], whose details are discussed in Ref. 63. Figure 16 shows the IXS measurement and the phonon spectral function calculation. The IXS spectrum shows an asymmetric function shape. The spectral function has multiple peaks due to the strong anharmonicity. Their agreement is well confirmed after the phonon spectral function is smeared by the energy resolution of the IXS measurement setting.

6. Lattice Thermal Conductivity Calculation

The LTC calculation is one of the most important applications of the first-principles phonon calculation. In this section, the LTC value or tensor is denoted by κ since it is a popular choice and probably it would not be confused with the label of atoms in the unit cell.

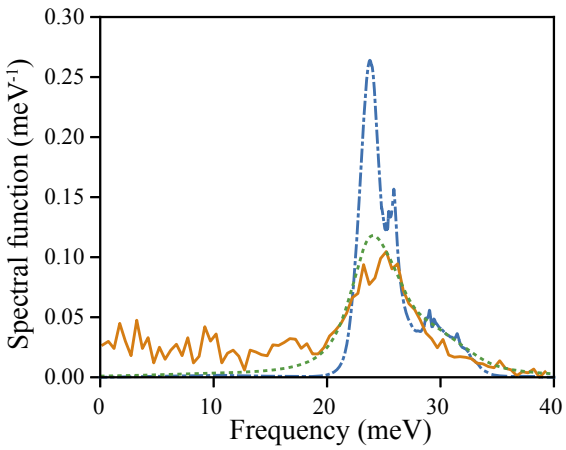

Fig. 16. (Color online) This figure is obtained from Ref. 63 licensed under CC-BY-4.0. The IXS measurement and calculated phonon spectral function of KCl at 300 K.[63] The IXS spectrum was measured at $\mathbf{Q} = (2.88\ 2.93\ -2.90)$ and the phonon spectral function was calculated at $\mathbf{q} = (0.097\ 0.097\ 0.097)$. These coordinates are represented with respect to reciprocal basis vectors of cubic lattice. The solid, dashed-dotted, and dotted curves show the IXS spectrum, phonon spectral function, and phonon spectral function smeared by the Lorentzian function with the 1.5 meV scale parameter, respectively. The energy of 1.5 meV is the energy resolution of the IXS measurement setting. Phonon frequency unit of meV is used in this figure where 1 meV–0.24 THz.

6.1 *Relaxation time approximation*

In the kinetic theory, LTC is written as[33,34]

$$\kappa = \frac{1}{NV_c}\sum_\lambda C_\lambda \mathbf{v}_\lambda \otimes \mathbf{v}_\lambda \tau_\lambda^{\mathrm{SMRT}}, \tag{48}$$

where $\tau_\lambda^{\mathrm{SMRT}}$ is the single-mode relaxation time (SMRT), and C_λ is the mode heat-capacity defined as

$$C_\lambda = \frac{\partial \hbar\omega_\lambda \left[n_\lambda(T) + \frac{1}{2} \right]}{\partial T} = k_{\mathrm{B}} \left(\frac{\hbar\omega_\lambda}{k_{\mathrm{B}}T} \right)^2 \frac{\exp(\hbar\omega_\lambda / k_{\mathrm{B}}T)}{[\exp(\hbar\omega_\lambda / k_{\mathrm{B}}T) - 1]^2}. \tag{49}$$

Equation (48) is obtained as the solution of the Peierls–Boltzmann equation under the relaxation time approximation (RTA).[31,32,91] C_λ and $\mathbf{v}_\lambda$ are computed from the harmonic

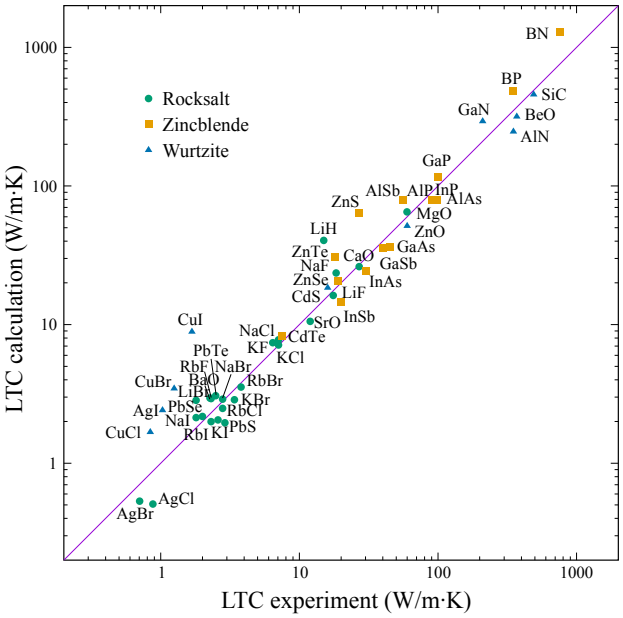

Fig. 17. (Color online) LTCs of rocksalt-type, zincblende-type, and wurtzite-type compounds at 300 K under the relaxation time approximation. The calculations and experiments are compared.

phonon calculation. Employing τ_λ as $\tau_\lambda^{\mathrm{SMRT}}$, Eq. (48) is calculated immediately.

In Fig. 17, LTCs of rocksalt-type, zincblende-type, and wurtzite-type compounds calculated at 300 K are compared with the experimental values. The calculations were performed with the similar computational details in Ref. 38 but GGA of PBEsol[60] and NAC by Gonze and Lee[15] were employed. Systematic agreement between calculations and experiments is observed, which exhibits strong predictability of the first-principles LTC calculation. The computational demand of the LTC calculation is non-trivial as explained in Sect. 5.1. Typically, the computational bottleneck of the LTC calculation is in the first-principles calculation of forces in many supercells with different configurations of displacements. When a primitive cell contains large number of atoms, the calculation of $\Phi_{\lambda\lambda'\lambda''}$ in Eq. (44) can be also a computational bottleneck due to heavy iteration over combinations of three atoms in the primitive cell.

Since Eq. (48) is a simple summation over phonon modes, the result of the LTC calculation is naturally analyzed in terms of phonon mode. As an example of the analysis, the LTC calculation performed in Ref. 92 is presented as follows. In this study, LTCs of SiO_2 polymorphs of α-quartz and α-cristobalite were compared. Both crystal structures are composed of SiO_4 tetrahedra connected by their vertices, but the connecting manners are different. Although their phonon DOS look similar as shown in Fig. 18, their calculated LTCs[92] are dissimilar as presented in Table I, where α-quartz exhibits highly anisotropic κ, whereas α-cristobalite shows rather isotropic κ.

To discuss phonon mode dependent properties related to LTC, a DOS-like-plot is often useful. For this purpose, we define $\kappa(\omega)$ by

$$\kappa(\omega) \equiv \frac{1}{N}\sum_\lambda \kappa_\lambda \delta(\omega - \omega_\lambda) \tag{50}$$

with

$$\kappa_\lambda = \frac{1}{V_c} C_\lambda \mathbf{v}_\lambda \otimes \mathbf{v}_\lambda \tau_\lambda, \tag{51}$$

so that

$$\kappa = \int_0^\infty \kappa(\omega)\, d\omega. \tag{52}$$

For the numerical calculation of $\kappa(\omega)$, the linear tetrahedron method is used in phono3py. In Fig. 19(a), $\kappa(\omega)$ of α-quartz and α-cristobalite calculated at 300 K are presented. We can see that low frequency phonons at $\omega < 5$ THz mostly contribute to the total LTCs of the both compounds. This is because phonon lifetimes of lower phonon frequency modes tend to be longer as shown in Fig. 19(b). Minor difference of the phonon lifetime distributions between α-quartz and α-cristobalite is observed. This is attributed mainly to the difference in their phonon DOS that are shown in Fig. 18.

Table I. Calculated lattice thermal conductivities κ (W/m-K) of α-quartz and α-cristobalite at 300 K.[92]

	Space-group type	$\kappa_{xx} = \kappa_{yy}$	κ_{zz}
α-quartz	$P3_221$	4.9	10.7
α-cristobalite	$P4_12_12$	6.4	7.6

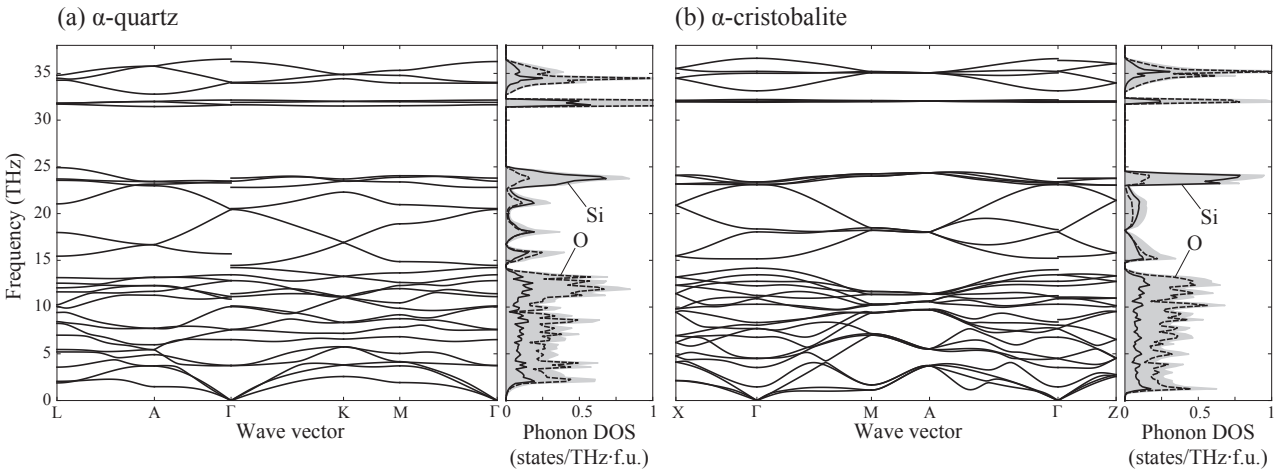

Fig. 18. These figures are obtained from Ref. 92 licensed under CC-BY-4.0. Phonon band structures and DOS of (a) α-quartz and (b) α-cristobalite.

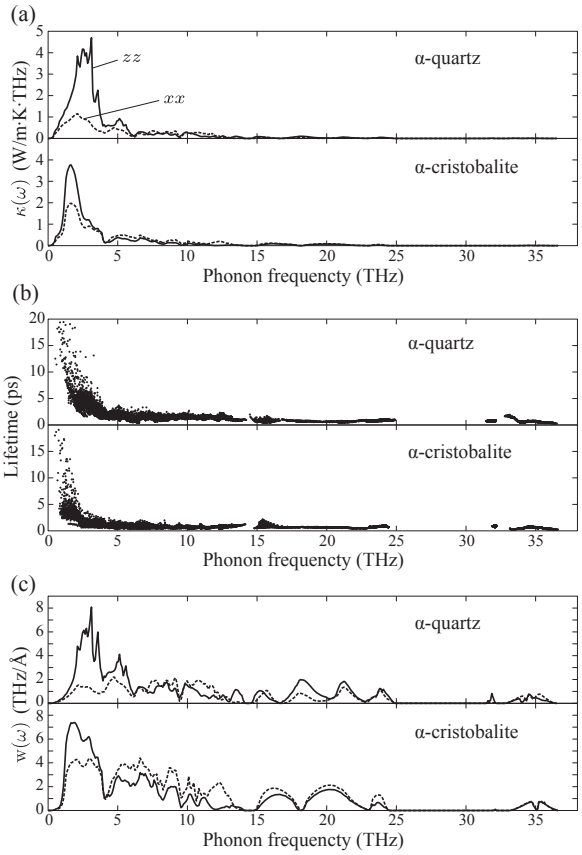

Fig. 19. These figures are obtained from Ref. 92 licensed under CC-BY-4.0. Microscopic analyses of LTCs of α-quartz and α-cristobalite. (a) Phonon mode contributions to LTCs [Eq. (50)] at 300 K. (b) Phonon lifetime distributions at 300 K. (c) Visualizations of impact of group velocity to LTCs [Eq. (53)].

The anisotropy of $\kappa(\omega)$ in α-quartz is observed clearly. This means that $\mathbf{v}_\lambda \otimes \mathbf{v}_\lambda$ is anisotropic in α-quartz. To visualize $\mathbf{v}_\lambda \otimes \mathbf{v}_\lambda$, a function $\mathrm{w}(\omega)$ similar to $\kappa(\omega)$ is defined as

$$\mathrm{w}(\omega) \equiv \frac{1}{N}\sum_\lambda \frac{1}{V_\mathrm{c}} \mathbf{v}_\lambda \otimes \mathbf{v}_\lambda \delta(\omega - \omega_\lambda). \tag{53}$$

In Fig. 19(c), $\mathrm{w}(\omega)$ of α-quartz and α-cristobalite are presented. The anisotropy of $\mathrm{w}(\omega)$ is more evident in α-quartz than α-cristobalite. This quantitative analysis is useful, since the anisotropy is difficult to recognize from the phonon band structure diagrams of Fig. 18, although the group velocity is the slope of the band structure.

Phonon mean free path (MFP) is an interesting quantity in LTC. Under SMRT, the phonon MFP is written as

$$\mathbf{l}_\lambda = \mathbf{v}_\lambda \tau_\lambda. \tag{54}$$

Integrating κ_λ over the phonon modes whose phonon MFPs are below a maximum phonon MFP, l_max, we may define $\kappa(l_\mathrm{max})$ as

$$\kappa(l_\mathrm{max}) = \int_0^{l_\mathrm{max}} \frac{1}{N}\sum_\lambda \kappa_\lambda \delta(l_\mathrm{MFP} - l_\lambda)\, dl_\mathrm{MFP}. \tag{55}$$

The calculated results of Eq. (55) for α-quartz and α-cristobalite at 300 K are shown in Fig. 20. This calculation was performed using the raw calculation data used in Ref. 92. The value similar to Eq. (50) may be rather useful, which is written as

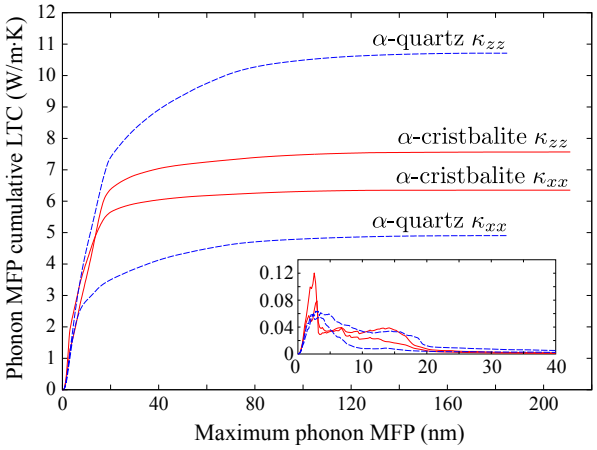

Fig. 20. (Color online) Cumulative LTCs with respect to phonon MFP [Eq. (55)] of α-quartz (dashed curves) and α-cristobalite (solid curves) at 300 K. The inset shows phonon MFP derivatives of the cumulative LTCs [Eq. (56)].

$$\kappa(l_\mathrm{MFP}) = \frac{1}{N}\sum_\lambda \kappa_\lambda \delta(l_\mathrm{MFP} - l_\lambda). \tag{56}$$

This indicates impact to LTC by phonon modes having specific values of phonon MFPs. The calculated results of Eq. (56) for α-quartz and α-cristobalite are shown in the inset of Fig. 20.

6.2 *Phonon-isotope scattering*

In the phono3py code, scattering rate of a phonon mode by randomly distributed isotopes is calculated using the second-order perturbation theory given by Tamura[93] as

$$\frac{1}{\tau_\lambda^\mathrm{iso}(\omega)} = \frac{\pi\omega_\lambda^2}{2N}\sum_{\lambda'}\delta(\omega - \omega_{\lambda'})\sum_\kappa g_\kappa \left|\sum_\alpha W_{\kappa\alpha}^*(\lambda')W_{\kappa\alpha}(\lambda)\right|^2. \tag{57}$$

In Eq. (57), g_κ is the mass variance parameter defined as

$$g_\kappa = \sum_i f_i \left(1 - \frac{m_{i\kappa}}{\sum_j f_j m_{j\kappa}}\right)^2, \tag{58}$$

where f_i and $m_{i\kappa}$ are the mole fraction and atomic weight of the ith isotope, respectively. To include phonon-isotope scattering into LTC, it is a reasonable approximation to employ the Matthiessen's rule for SMRT as follows:

$$\frac{1}{\tau_\lambda^\mathrm{total}} = \frac{1}{\tau_\lambda} + \frac{1}{\tau_\lambda^\mathrm{iso}(\omega_\lambda)}. \tag{59}$$

The impact of phonon-isotope scattering is larger for phonon modes having longer phonon lifetimes. The same calculation as shown in Fig. 17 was performed including the phonon-isotope scattering, where atomic weights of elements of Ref. 94 were used. Figure 21 shows the ratio of LTCs of the compounds with and without isotope effect.

6.3 *Direct solution to linearized phonon Boltzmann equation*

Using a direct solution of the linearized phonon Boltzmann equation (LBTE) by Chaput,[95] LTC is written as

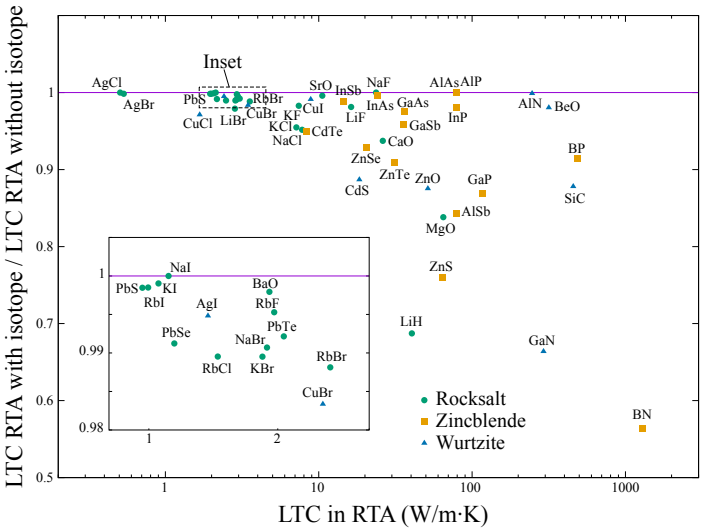

Fig. 21. (Color online) Ratios of LTCs of the same compounds as those in Fig. 17 at 300 K calculated under the relaxation time approximation with and without including the phonon-isotope scattering of Eq. (57).

$$\kappa_{\alpha\alpha'} = \frac{1}{4k_{\mathrm{B}}T^2NV_{\mathrm{c}}}\sum_{\lambda\lambda'}\frac{\hbar\omega_\lambda v_{\lambda,\alpha}}{\sinh\left(\frac{\hbar\omega_\lambda}{2k_{\mathrm{B}}T}\right)}(\Omega^{\sim1})_{\lambda\lambda'}\frac{\hbar\omega_{\lambda'}v_{\lambda',\alpha'}}{\sinh\left(\frac{\hbar\omega_{\lambda'}}{2k_{\mathrm{B}}T}\right)}, \tag{60}$$

where Ω is the collision matrix proposed in Ref. 95:

$$\Omega_{\lambda\lambda'} = \delta_{\lambda\lambda'}\frac{1}{\tau_\lambda} + \frac{36\pi}{\hbar^2}\sum_{\lambda''}|\Phi_{\lambda\lambda'\lambda''}|^2\frac{1}{\sinh\left(\frac{\hbar\omega_{\lambda''}}{2k_{\mathrm{B}}T}\right)} \times[\delta(\omega_\lambda-\omega'_\lambda-\omega''_\lambda) + \delta(\omega_\lambda+\omega'_\lambda-\omega''_\lambda)+\delta(\omega_\lambda-\omega'_\lambda+\omega''_\lambda)]. \tag{61}$$

Ω is a symmetric positive-semidefinite matrix, and $\Omega^{\sim1}$ means the Moore–Penrose inverse of the collision matrix Ω. To achieve reasonable convergence of LTC with respect to $\mathbf{q}$-point sampling density, the matrix size of Ω tends to become large, and its computation of the inversion can require a huge memory space and computing time. Utilizing crystal symmetry, the pair of Eqs. (60) and (61) is transformed to a compact form as presented in the same paper by Chaput.[95] The compact collision matrix is given as

$$\tilde{\Omega}_{\tilde{\mathbf{q}}\nu\alpha,\tilde{\mathbf{q}}'\nu'\alpha'} = \frac{1}{\sqrt{g_{\tilde{\mathbf{q}}}g_{\tilde{\mathbf{q}}'}}}\sum_{\mathrm{R}\in\mathrm{P}}R_{\alpha\alpha'}\Omega_{\tilde{\mathbf{q}}\nu,\mathrm{R}\tilde{\mathbf{q}}'\nu'}, \tag{62}$$

where $\tilde{\mathbf{q}}$ is the wave vector in the irreducible part of BZ, R is the rotational operation in the crystallographic point group P, and $g_{\tilde{\mathbf{q}}}$ is the order of the point group at the wave vector $\tilde{\mathbf{q}}$ (little co-group). With $\tilde{\Omega}$, Eq. (60) is written as

$$\kappa_{\beta\beta'} = \frac{1}{4k_{\mathrm{B}}T^2NV_{\mathrm{c}}} \times\sum_{\substack{\tilde{\mathbf{q}}\nu\alpha\\ \tilde{\mathbf{q}}'\nu'\alpha'}}\frac{\hbar\omega_{\tilde{\mathbf{q}}\nu}v_{\tilde{\mathbf{q}}\nu,\alpha}}{\sinh\left(\frac{\hbar\omega_{\tilde{\mathbf{q}}\nu}}{2k_{\mathrm{B}}T}\right)}\frac{[\tilde{\Omega}^{\sim1}\mathrm{I}(\beta,\beta')]_{\tilde{\mathbf{q}}\nu\alpha,\tilde{\mathbf{q}}'\nu'\alpha'}}{\sqrt{g_{\tilde{\mathbf{q}}}g_{\tilde{\mathbf{q}}'}}}\frac{\hbar\omega_{\tilde{\mathbf{q}}'\nu'}v_{\tilde{\mathbf{q}}'\nu',\alpha'}}{\sinh\left(\frac{\hbar\omega_{\tilde{\mathbf{q}}'\nu'}}{2k_{\mathrm{B}}T}\right)}, \tag{63}$$

where $\mathrm{I}(\beta,\beta')$ is the matrix to expand vectors in the irreducible BZ to those in the full BZ written as

$$I_{\tilde{\mathbf{q}}\nu\alpha,\tilde{\mathbf{q}}'\nu'\alpha'}(\beta,\beta') = \delta_{\mathbf{q},\mathbf{q}'}\delta_{\nu,\nu'}\sum_{\mathrm{R}\in\mathrm{P}}\frac{R_{\beta\alpha}R_{\beta'\alpha'}+R_{\beta'\alpha}R_{\beta\alpha'}}{2}. \tag{64}$$

Note that $\tilde{\Omega}_{\tilde{\mathbf{q}}\nu\alpha,\tilde{\mathbf{q}}'\nu'\alpha'} = \tilde{\Omega}_{\tilde{\mathbf{q}}\nu\alpha',\tilde{\mathbf{q}}'\nu'\alpha}$ because of general property of group. This allows to choose the symmetric form $\mathrm{I}(\beta,\beta') = \mathrm{I}(\beta',\beta)$ of Eq. (64), by which we get $\kappa_{\beta\beta'} = \kappa_{\beta'\beta}$.[95] At least currently, this compact form is essential to achieve reasonable convergence of LTC under the direct solution of LBTE for many compounds.

The same calculation as shown in Fig. 17 was performed under the direct solution of LBTE instead of RTA at 300 K as shown in Fig. 22. The results are compared with those of RTA. Large increases of LTCs as the ratios are observed for a few compounds, though most of the compounds exhibit minor increases of LTCs.

7. Automation of First-principles Phonon Calculations

We should be able to compute more and more phonon properties utilizing modern computer power. To achieve it, we want to perform workflow of the first-principles phonon calculation in an automated fashion. There are different types of the automation techniques. One may be easy to set up the system but less scalable. The other may require building a complicated system but more failure tolerant and scalable against large data. In either case, the workflow of the first-principles phonon calculation itself is simple, and its automation has been already achieved at a certain level.

Two important use-cases of the automated first-principles phonon calculations are handling many phonon calculations and executing specific algorithms that involve different types of calculation codes. The required capabilities for automation system to perform them are the robustness and systematic

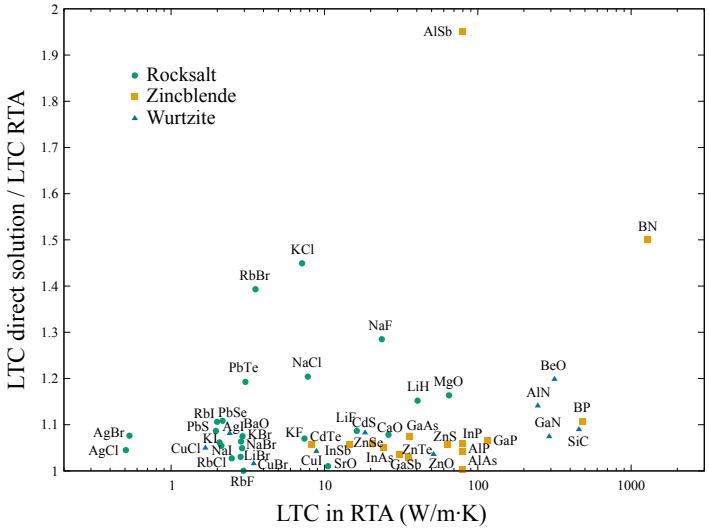

Fig. 22. (Color online) Ratios of LTCs of the same compounds as those in Fig. 17 at 300 K calculated under the direct solution[95] and the relaxation time approximation.

data handling. Fortunately, we have several choices of open-source-software environments to automate scientific computer simulations, which are so-called workflow engines. In this section, a typical workflow of the first-principles phonon calculation and its applications performed using workflow engines are presented.

7.1 First-principles phonon calculation workflow

A typical workflow of the first-principles phonon calculation with the finite-displacement supercell approach is outlined as follows:

1. Prepare a crystal structure model of unit cell that is standardized following a crystallographic convention
2. Relax the geometry of the crystal structure model using first-principles calculation until residual forces on atoms become close to zero
3. Create supercells with finite displacements
4. Calculate forces of atoms in the supercells of the step 3 using first-principles calculation
5. Calculate supercell force constants using displacements of the step 3 and forces of the step 4
6. Calculate phonon properties from the supercell force constants of the step 5

This workflow is illustrated in Fig. 23. It is important that the input crystal structure model has been standardized in terms of crystal symmetry[96] for the later systematic handling of the calculation data. Usually, this workflow is performed by using two or three different calculation codes: first-principles calculation code, phonon calculation code, and optionally force-constants calculation code. For the harmonic phonon calculation, the first-principles calculations are executed on a powerful computer such as supercomputer, computing cluster, etc. and the other calculations are often processed on a normal personal computer. For the LTC calculations, all the calculation steps may be performed on a powerful computer.

7.2 Automated phonon calculation workflow

Currently, workflows for automation of the phonopy and phono3py codes are provided as the AiiDA plugins.[97]

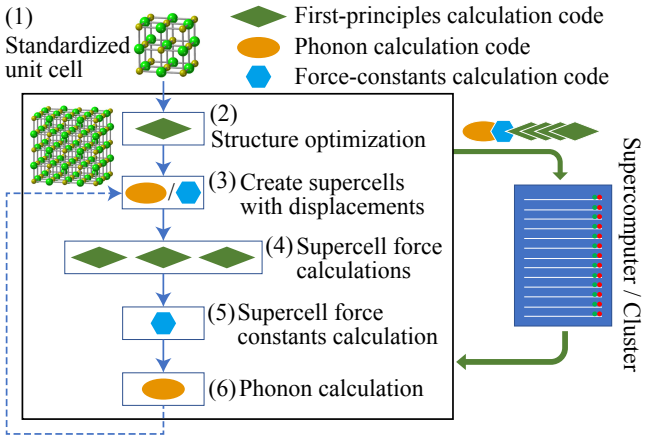

Fig. 23. (Color online) An illustration of workflow of the first-principles phonon calculation with the finite-displacement supercell approach.

AiiDA[98,99] is an environment that provides workflow engine and flexible database system. The latter stores not only the data but also the flows of processes and data. As an example, the phonopy workflow graph of a harmonic phonon calculation auto-generated by AiiDA is shown in Fig. 24. Inside the phonopy workflow, the VASP workflows[100] are called to run the first-principles calculations to obtain forces of atoms in supercells for supercell force constants calculation and Born effective charges and dielectric constant tensor required for NAC. Using these intermediate data, phonon properties are calculated after the supercell force constants calculation. The final results are attached to end points of the phonopy workflow as the data nodes.

All the intermediate data inside the AiiDA workflow are stored in the AiiDA database as immutable data, i.e., those data are not allowed to be modified or removed once they are created. The dataflow has to be designed to be an acyclic directed graph. These restrictions of the AiiDA workflow help the automated calculation reproducible and the history traceable along the process and data flows.

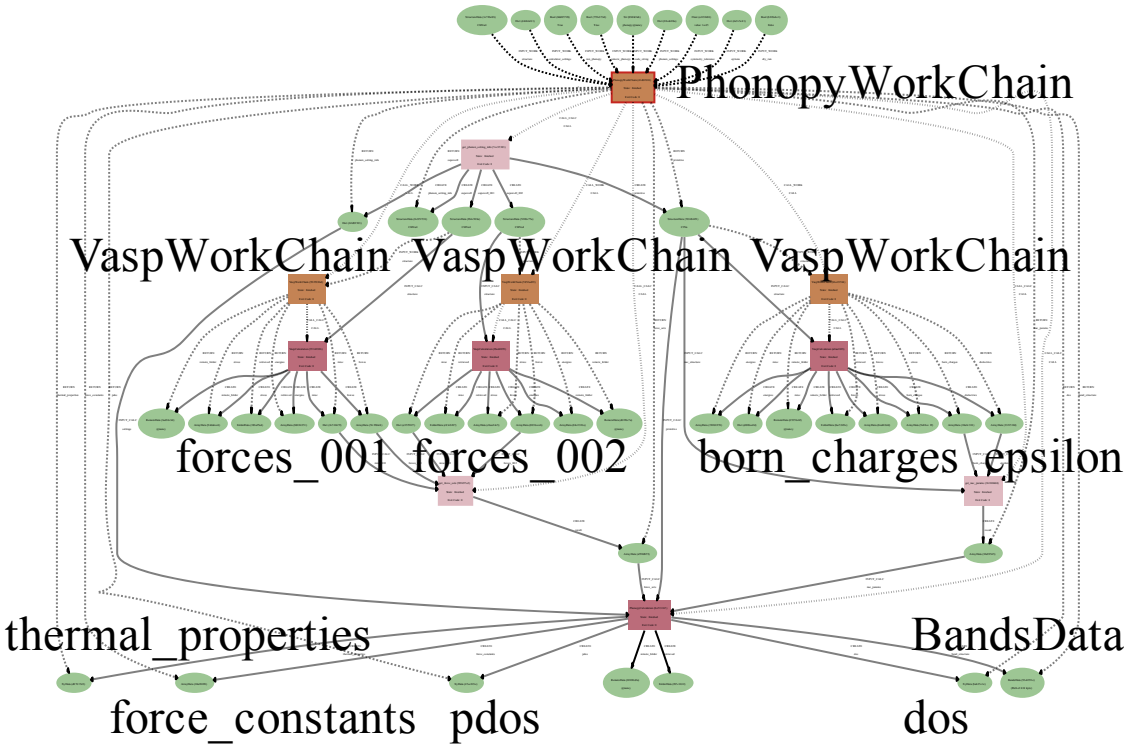

Fig. 24. (Color online) An example of the phonon calculation workflow automated by AiiDA.[98,99] The calculations in the workflow were performed using the phonopy[26] and VASP codes.[2–4] The figure was auto-generated by AiiDA, where some texts were highlighted manually. Circles and boxes indicate the data and process nodes, respectively. Curves connecting the nodes show the process and data flows.

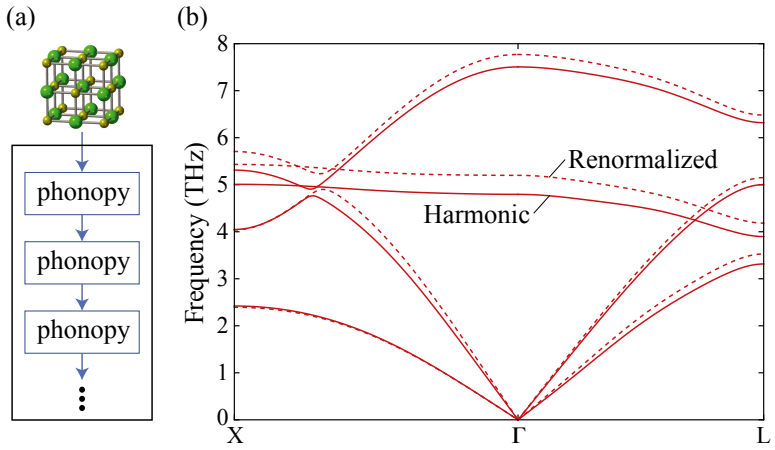

Fig. 25. (Color online) (a) Illustration of the workflow that iterates the phonopy workflow. (b) Phonon band structures of NaCl calculated under the harmonic approximation (solid curves) and the stochastic self-consistent harmonic approximation at 300 K (dashed curves). These phonon band structures were calculated using the raw data of the phonon calculations used in Ref. 63.

7.3 Iteration of harmonic phonon calculations

Like that the VASP workflow is called in the phonopy workflow of Fig. 24, the phonopy workflow can be also called by another workflow. The dotted line connecting from the step 6 to 3 in Fig. 23 means iteration of the phonopy workflow by calling itself using the phonon calculation output as the input of the next phonon calculation. Since the cyclic data flow is prohibited in AiiDA, this algorithm is implemented as another workflow that iterates the phonopy workflow processes as shown in Fig. 25(a).

This workflow was used to study strong anharmonicity of KCl and NaCl in Ref. 63 to include finite temperature effect in the supercell force constants. In this study, random displacements were sampled in phonon coordinates following harmonic oscillator distribution function at 300 K, and displacements were introduced in the supercells. Harmonic supercell force constants were calculated by least-squares fitting using the ALM code.[46] Since finally obtained supercell force constants are considered equivalent to those of SSCHA,[41] this procedure was iterated until SSCHA free energies became converged. The renormalized phonon band structure of NaCl is shown in Fig. 25(b). Increasing temperatures, atoms vibrate with larger amplitude and hit the anharmonic potential energy surface. In Fig. 26, distributions of SSCHA random displacement distances of atoms in NaCl at 300 K are presented. Most of displacement distances are far

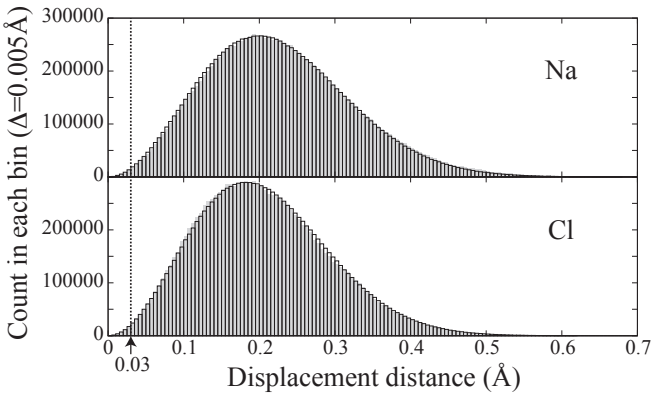

Fig. 26. Displacement distributions of atoms in NaCl at 300 K presented as histograms by solid boxes with 200 bins below 0.7 Å. Random displacements were sampled in phonon coordinates following harmonic oscillator distribution function,[63] and displacement distances were measured in supercells in direct coordinates. The renormalized harmonic supercell force constants of Ref. 63 were used to generate 50000 randomly displaced supercells, where each supercell has 256 Na and 256 Cl atoms. Shaded histograms show displacement distributions obtained from an NVT molecular dynamics (MD) calculation with 3200 steps using the VASP code. The count in each bin of the histogram from the MD calculation is normalized to that of the phonon calculation. The histograms by the phonon and MD calculations look identical, but slightly different.

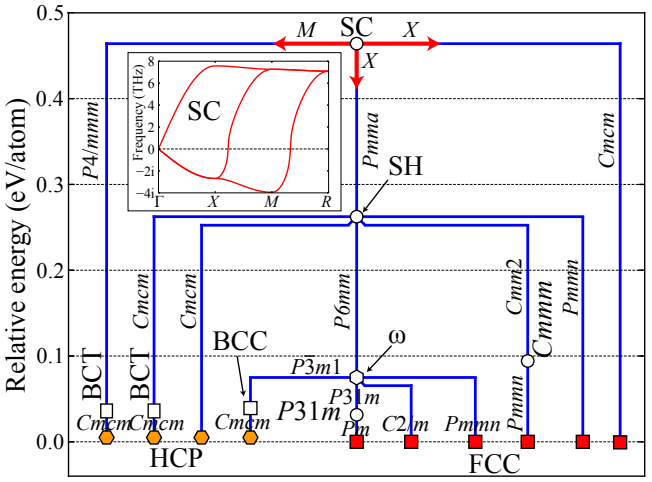

Fig. 27. (Color online) This figure is obtained from Ref. 26 licensed under CC-BY-4.0. Transition pathway of Cu from simple cubic (SC) structure.[114] The inset shows phonon band structure of SC Cu. The SC structure is relaxed following eigenvectors of phonon modes that exhibit imaginary phonon frequencies at commensurate points. Dynamical stabilities of crystal structures obtained after the relaxations (SH, ω, BCC, ···) are examined by the first-principles phonon calculation. The same procedure is repeated recursively until all relaxed crystal structures at end points are found to be dynamically stable. In this algorithm, not only crystal structures are explored, but also the structural relationships among the crystal structural phases are determined.

larger than 0.03 Å that was used to calculate harmonic phonon band structure shown in Fig. 25(b). For the comparison, an NVT MD calculation using the VASP code was performed and it was confirmed that similar distributions of displacements were generated. This MD calculation used the same 512 atoms supercell with loose convergence parameters.

7.4 *Execution of many phonon calculations*

Many crystal structures can be obtained through materials or crystallographic database services such as the Materials Project,[101] the Crystallography Open Database (COD)[102–108] and the theoretical COD.[109] It is straightforward to apply the automated phonon calculation to high-throughput phonon calculation of crystal structures obtained from these database.

Using an automated phonon calculation, Togo et al. developed a phonon calculation database,[110] where the first-principles phonon calculations of more than 10000 crystal structures were performed using the phonopy and VASP codes. For the high-throughput first-principles phonon calculation, initial crystal structures were obtained from the Materials Project via the materials application programming interface using the pymatgen code.[101,111] Since the Materials Project database provides not only the crystal structures but also the calculated electronic structure information, utilizing the materials information, non-metallic and non-magnetic crystals were selected. Crystal structures having primitive cells that contain large number of atoms were excluded from the list of the target crystal structures since large computational resource required by them was considered unaffordable.

The calculated data that can be used as the input of the phonopy code are distributed at the phonon calculation database. It is planned to migrate the phonon calculation database to the other materials data repository service because of the difficulty of maintaining current database server. The raw output data that were generated using an obsolete workflow engine[112] will be exported to the AiiDA database to open the data at the Materials Cloud.[113]

7.5 *Recursive search of phase transition pathways*

An automated phonon calculation was used for the structural transition pathway search. In the study of Cu in Ref. 114, different structural phases were related by phonon modes that exhibit structural instabilities as shown in Fig. 27. The implemented algorithm is straightforward, where the phonon calculations were used to examine dynamical stabilities of crystal structures. Choosing a crystal structure that has high crystal symmetry (SC in Fig. 27), when imaginary phonon frequencies are found as shown in the inset of Fig. 27, the symmetry of the crystal structure is lowered by introducing atomic displacements corresponding to the eigenvector. Since the imaginary phonon frequency indicates negative curvature of the potential energy surface along the phonon coordinate, with a little push in the phonon coordinate, the crystal structure starts to relax. The geometry of the crystal structure is relaxed by the first-principles calculation along the symmetry constrained pathway [e.g., SC → *Pmma* → simple hexagonal (SH)]. Next, dynamical stability of the relaxed crystal structure (SH) is examined by the phonon calculation. When a phonon calculation exhibits multiple imaginary phonon frequencies, the multiple routes (e.g., three branches from SC) are pursued. This procedure is repeated recursively until all the crystal structures at the end points become dynamically stable. An automated phonon calculation workflow was developed for this study to perform this algorithm. Since this workflow was implemented on an obsolete workflow engine,[112] it is planned to re-implement it for AiiDA.

8. Summary

The first-principles phonon calculation with the finite displacement supercell approach implemented in the the phonopy and phono3py codes were reviewed. Harmonic, quasi-harmonic, and anharmonic phonon calculations were explained using the formulae and their calculation examples. To utilize modern computer power effectively, automation of the phonon calculation became essential. Therefore, the workflow of the first-principles phonon calculation was briefly described. A few applications of the automated phonon calculation workflow were presented. The raw data of some calculation examples will be opened in the public domain, which will be informed at the phonopy's website.

Acknowledgments This work was supported by MEXT Japan through ESISM (Elements Strategy Initiative for Structural Materials) of Kyoto University and JSPS KAKENHI Grant Number JP21K04632.

*togo.atsushi@gmail.com

1) *Electronic Structure*, ed. R. M. Martin (Cambridge University Press, Cambridge, U.K., 2004).
2) G. Kresse, J. Non-Cryst. Solids **192–193**, 222 (1995).
3) G. Kresse and J. Furthmüller, Comput. Mater. Sci. **6**, 15 (1996).
4) G. Kresse and D. Joubert, Phys. Rev. B **59**, 1758 (1999).
5) P. Giannozzi, S. Baroni, N. Bonini, M. Calandra, R. Car, C. Cavazzoni, D. Ceresoli, G. L. Chiarotti, M. Cococcioni, I. Dabo, A. D. Corso, S. de Gironcoli, S. Fabris, G. Fratesi, R. Gebauer, U. Gerstmann, C. Gougoussis, A. Kokalj, M. Lazzeri, L. Martin-Samos, N. Marzari, F. Mauri, R. Mazzarello, S. Paolini, A. Pasquarello, L. Paulatto, C. Sbraccia, S. Scandolo, G. Sclauzero, A. P. Seitsonen, A. Smogunov, P. Umari, and R. M. Wentzcovitch, J. Phys.: Condens. Matter **21**, 395502 (2009).
6) P. Giannozzi, O. Andreussi, T. Brumme, O. Bunau, M. B. Nardelli, M. Calandra, R. Car, C. Cavazzoni, D. Ceresoli, M. Cococcioni, N. Colonna, I. Carnimeo, A. D. Corso, S. de Gironcoli, P. Delugas, R. A. DiStasio, A. Ferretti, A. Floris, G. Fratesi, G. Fugallo, R. Gebauer, U. Gerstmann, F. Giustino, T. Gorni, J. Jia, M. Kawamura, H.-Y. Ko, A. Kokalj, E. Küçükbenli, M. Lazzeri, M. Marsili, N. Marzari, F. Mauri, N. L. Nguyen, H.-V. Nguyen, A. O. de-la Roza, L. Paulatto, S. Poncé, D. Rocca, R. Sabatini, B. Santra, M. Schlipf, A. P. Seitsonen, A. Smogunov, I. Timrov, T. Thonhauser, P. Umari, N. Vast, X. Wu, and S. Baroni, J. Phys.: Condens. Matter **29**, 465901 (2017).
7) Top500 project, https://www.top500.org/statistics/perfdevel/ (2022).
8) Wikipedia, top500, Data obtained at https://en.wikipedia.org/wiki/TOP500. Accessed on 19th Apr. 2022.
9) P. Hohenberg and W. Kohn, Phys. Rev. **136**, B864 (1964).
10) W. Kohn and L. J. Sham, Phys. Rev. **140**, A1133 (1965).
11) S. Baroni, P. Giannozzi, and A. Testa, Phys. Rev. Lett. **58**, 1861 (1987).
12) X. Gonze and J.-P. Vigneron, Phys. Rev. B **39**, 13120 (1989).
13) P. Giannozzi, S. de Gironcoli, P. Pavone, and S. Baroni, Phys. Rev. B **43**, 7231 (1991).
14) S. Y. Savrasov, Phys. Rev. B **54**, 16470 (1996).
15) X. Gonze and C. Lee, Phys. Rev. B **55**, 10355 (1997).
16) S. Baroni, S. de Gironcoli, A. Dal Corso, and P. Giannozzi, Rev. Mod. Phys. **73**, 515 (2001).
17) K. Parlinski, Z. Q. Li, and Y. Kawazoe, Phys. Rev. Lett. **78**, 4063 (1997).
18) D. Alfè, Comput. Phys. Commun. **180**, 2622 (2009).
19) T. Tadano, Y. Gohda, and S. Tsuneyuki, J. Phys.: Condens. Matter **26**, 225402 (2014).
20) T. Tadano and S. Tsuneyuki, Phys. Rev. B **92**, 054301 (2015).
21) Y. Oba, T. Tadano, R. Akashi, and S. Tsuneyuki, Phys. Rev. Mater. **3**, 033601 (2019).
22) Y. Wang, L.-Q. Chen, and Z.-K. Liu, Comput. Phys. Commun. **185**, 2950 (2014).
23) O. Hellman, I. A. Abrikosov, and S. I. Simak, Phys. Rev. B **84**, 180301 (2011).
24) O. Hellman and I. A. Abrikosov, Phys. Rev. B **88**, 144301 (2013).
25) O. Hellman, P. Steneteg, I. A. Abrikosov, and S. I. Simak, Phys. Rev. B **87**, 104111 (2013).
26) A. Togo and I. Tanaka, Scr. Mater. **108**, 1 (2015).
27) X. Gonze, B. Amadon, G. Antonius, F. Arnardi, L. Baguet, J.-M. Beuken, J. Bieder, F. Bottin, J. Bouchet, E. Bousquet, N. Brouwer, F. Bruneval, G. Brunin, T. Cavignac, J.-B. Charraud, W. Chen, M. Côté, S. Cottenier, J. Denier, G. Geneste, P. Ghosez, M. Giantomassi, Y. Gillet, O. Gingras, D. R. Hamann, G. Hautier, X. He, N. Helbig, N. Holzwarth, Y. Jia, F. Jollet, W. Lafargue-Dit-Hauret, K. Lejaeghere, M. A. L. Marques, A. Martin, C. Martins, H. P. C. Miranda, F. Naccarato, K. Persson, G. Petretto, V. Planes, Y. Pouillon, S. Prokhorenko, F. Ricci, G.-M. Rignanese, A. H. Romero, M. M. Schmitt, M. Torrent, M. J. van Setten, B. V. Troeye, M. J. Verstraete, G. Zérah, and J. W. Zwanziger, Comput. Phys. Commun. **248**, 107042 (2020).
28) A. H. Romero, D. C. Allan, B. Amadon, G. Antonius, T. Applencourt, L. Baguet, J. Bieder, F. Bottin, J. Bouchet, E. Bousquet, F. Bruneval, G. Brunin, D. Caliste, M. Côté, J. Denier, C. Dreyer, P. Ghosez, M. Giantomassi, Y. Gillet, O. Gingras, D. R. Hamann, G. Hautier, F. Jollet, G. Jomard, A. Martin, H. P. C. Miranda, F. Naccarato, G. Petretto, N. A. Pike, V. Planes, S. Prokhorenko, T. Rangel, F. Ricci, G.-M. Rignanese, M. Royo, M. Stengel, M. Torrent, M. J. van Setten, B. V. Troeye, M. J. Verstraete, J. Wiktor, J. W. Zwanziger, and X. Gonze, J. Chem. Phys. **152**, 124102 (2020).
29) X. Gonze, J.-M. Beuken, R. Caracas, F. Detraux, M. Fuchs, G.-M. Rignanese, L. Sindic, M. Verstraete, G. Zerah, F. Jollet, M. Torrent, A. Roy, M. Mikami, P. Ghosez, J.-Y. Raty, and D. Allan, Comput. Mater. Sci. **25**, 478 (2002).
30) The Elk Code, http://elk.sourceforge.net/ (2022).
31) R. E. Peierls, Ann. Phys. **395**, 1055 (1929).
32) R. E. Peierls, *Quantum Theory of Solids* (Oxford University Press, Oxford, U.K., 2001).
33) J. M. Ziman, *Electrons and Phonons: The Theory of Transport Phenomena in Solids* (Oxford University Press, Oxford, U.K., 1960).
34) G. P. Srivastava, *Physics of Phonons* (CRC Press, Boca Raton, FL, 1990).
35) W. Li, J. Carrete, N. A. Katcho, and N. Mingo, Comput. Phys. Commun. **185**, 1747 (2014).
36) J. Carrete, B. Vermeersch, A. Katre, A. van Roekeghem, T. Wang, G. K. Madsen, and N. Mingo, Comput. Phys. Commun. **220**, 351 (2017).
37) A. Chernatynskiy and S. R. Phillpot, Comput. Phys. Commun. **192**, 196 (2015).
38) A. Togo, L. Chaput, and I. Tanaka, Phys. Rev. B **91**, 094306 (2015).
39) I. Errea, M. Calandra, and F. Mauri, Phys. Rev. Lett. **111**, 177002 (2013).
40) P. Souvatzis, O. Eriksson, M. I. Katsnelson, and S. P. Rudin, Phys. Rev. Lett. **100**, 095901 (2008).
41) A. van Roekeghem, J. Carrete, and N. Mingo, Comput. Phys. Commun. **263**, 107945 (2021).
42) L. Monacelli, R. Bianco, M. Cherubini, M. Calandra, I. Errea, and F. Mauri, J. Phys.: Condens. Matter **33**, 363001 (2021).
43) I. Errea, M. Calandra, and F. Mauri, Phys. Rev. B **89**, 064302 (2014).
44) R. Bianco, I. Errea, L. Paulatto, M. Calandra, and F. Mauri, Phys. Rev. B **96**, 014111 (2017).
45) L. Monacelli, I. Errea, M. Calandra, and F. Mauri, Phys. Rev. B **98**, 024106 (2018).
46) T. Tadano and S. Tsuneyuki, J. Phys. Soc. Jpn. **87**, 041015 (2018).
47) F. Eriksson, E. Fransson, and P. Erhart, Adv. Theory Simul. **2**, 1800184 (2019).
48) M. Born and K. Huang, *Dynamical Theory of Crystal Lattices* (Oxford University Press, Oxford, U.K., 1954).
49) *Dynamical Properties of Solids*, ed. G. K. Horton and A. A. Maradudin (North-Holland, Amsterdam, 1974) Vol. 1.
50) D. C. Wallace, *Thermodynamics of Crystals* (Dover, New York, 1998).
51) M. T. Dove, *Introduction to Lattice Dynamics* (Cambridge University Press, Cambridge, U.K., 1993).
52) G. Grimvall, *Thermophysical Properties of Materials* (Elsevier Science B.V., Amsterdam, 1999).
53) A. A. Maradudin and S. H. Vosko, Rev. Mod. Phys. **40**, 1 (1968).

54) M. El-Batanouny and F. Wooten, *Symmetry and Condensed Matter Physics: A Computational Approach* (Cambridge University Press, Cambridge, U.K., 2010).
55) P. Jacobs, *Group Theory with Applications in Chemical Physics* (Cambridge University Press, Cambridge, U.K., 2005).
56) E. Anderson, Z. Bai, C. Bischof, S. Blackford, J. Demmel, J. Dongarra, J. Du Croz, A. Greenbaum, S. Hammarling, A. McKenney, and D. Sorensen, *LAPACK Users' Guide* (SIAM, Philadelphia, PA, 1999) 3rd ed.
57) C. R. Harris, K. J. Millman, S. J. van der Walt, R. Gommers, P. Virtanen, D. Cournapeau, E. Wieser, J. Taylor, S. Berg, N. J. Smith, R. Kern, M. Picus, S. Hoyer, M. H. van Kerkwijk, M. Brett, A. Haldane, J. F. del Río, M. Wiebe, P. Peterson, P. Gérard-Marchant, K. Sheppard, T. Reddy, W. Weckesser, H. Abbasi, C. Gohlke, and T. E. Oliphant, Nature **585**, 357 (2020).
58) R. Shankar, *Principles of Quantum Mechanics* (Springer, Berlin, 1994).
59) A. Togo, L. Chaput, I. Tanaka, and G. Hug, Phys. Rev. B **81**, 174301 (2010).
60) J. P. Perdew, A. Ruzsinszky, G. I. Csonka, O. A. Vydrov, G. E. Scuseria, L. A. Constantin, X. Zhou, and K. Burke, Phys. Rev. Lett. **100**, 136406 (2008).
61) R. M. Pick, M. H. Cohen, and R. M. Martin, Phys. Rev. B **1**, 910 (1970).
62) X. Gonze, J.-C. Charlier, D. C. Allan, and M. P. Teter, Phys. Rev. B **50**, 13035 (1994).
63) A. Togo, H. Hayashi, T. Tadano, S. Tsutsui, and I. Tanaka, J. Phys.: Condens. Matter, **34**, 365401 (2022).
64) C. Kittel, *Introduction to Solid State Physics* (Wiley, New York, 1996) Vol. 7.
65) A. H. MacDonald, S. H. Vosko, and P. T. Coleridge, J. Phys. C **12**, 2991 (1979).
66) P. E. Blöchl, O. Jepsen, and O. K. Andersen, Phys. Rev. B **49**, 16223 (1994).
67) N. J. Lane, S. C. Vogel, G. Hug, A. Togo, L. Chaput, L. Hultman, and M. W. Barsoum, Phys. Rev. B **86**, 214301 (2012).
68) V. L. Deringer, R. P. Stoffel, A. Togo, B. Eck, M. Meven, and R. Dronskowski, CrystEngComm **16**, 10907 (2014).
69) K. Momma and F. Izumi, J. Appl. Crystallogr. **44**, 1272 (2011).
70) A crystal and molecular structures program for mac and windows, http://www.crystalmaker.com/ (2022).
71) G. L. Squires, *Introduction to the Theory of Thermal Neutron Scattering* (Cambridge University Press, Cambridge, U.K., 2012).
72) N. W. Ashcroft and N. D. Mermin, *Solid State Physics* (Thomson Learning, New York, 1976).
73) D. Waasmaier and A. Kirfel, Acta Crystallogr., Sect. A **51**, 416 (1995).
74) A. Togo, H. Hayashi, T. Tadano, S. Tsutsui, and I. Tanaka, J. Phys.: Condens. Matter **34**, 365401 (2022).
75) M. W. Chase, Jr., *NIST-JANAF Thermochemical Tables* (American Institute of Physics, New York, 1998) Journal of Physical and Chemical Reference Data Monographs.
76) M. I. Aroyo, A. Kirov, C. Capillas, J. M. Perez-Mato, and H. Wondratschek, Acta Crystallogr., Sect. A **62**, 115 (2006).
77) P. Vinet, J. H. Rose, J. Ferrante, and J. R. Smith, J. Phys.: Condens. Matter **1**, 1941 (1989).
78) A. J. C. Wilson, Proc. Phys. Soc. **53**, 235 (1941).
79) F. C. Nix and D. MacNair, Phys. Rev. **60**, 597 (1941).
80) A. G. Crocker and M. Bevis, in *The Science, Technology and Application of Titanium*, ed. R. I. Jaffee and N. E. Promisel (Pergamon, New York, 1970) p. 453.
81) A. Togo, Y. Inoue, and I. Tanaka, Phys. Rev. B **102**, 024106 (2020).
82) L. Chaput, A. Togo, I. Tanaka, and G. Hug, Phys. Rev. B **84**, 094302 (2011).
83) A. A. Maradudin and A. E. Fein, Phys. Rev. **128**, 2589 (1962).
84) G. D. Mahan, *Many-Particle Physics* (Springer, Berlin, 2000).
85) H. Bruus and K. Flensberg, *Many-Body Quantum Theory in Condensed Matter Physics: An Introduction* (Oxford University Press, Oxford, U.K., 2004).
86) L. Paulatto, I. Errea, M. Calandra, and F. Mauri, Phys. Rev. B **91**, 054304 (2015).
87) R. Bianco, I. Errea, M. Calandra, and F. Mauri, Phys. Rev. B **97**, 214101 (2018).
88) G. A. S. Ribeiro, L. Paulatto, R. Bianco, I. Errea, F. Mauri, and M. Calandra, Phys. Rev. B **97**, 014306 (2018).
89) U. Aseginolaza, R. Bianco, L. Monacelli, L. Paulatto, M. Calandra, F. Mauri, A. Bergara, and I. Errea, Phys. Rev. B **100**, 214307 (2019).
90) G. Raunio and L. Almqvist, Phys. Status Solidi B **33**, 209 (1969).
91) P. B. Allen and V. Perebeinos, Phys. Rev. B **98**, 085427 (2018).
92) K. Mizokami, A. Togo, and I. Tanaka, Phys. Rev. B **97**, 224306 (2018).
93) S.-i. Tamura, Phys. Rev. B **27**, 858 (1983).
94) J. R. de Laeter, J. K. Böhlke, P. De Bièvre, H. Hidaka, H. S. Peiser, K. J. R. Rosman, and P. D. P. Taylor, Pure Appl. Chem. **75**, 683 (2003).
95) L. Chaput, Phys. Rev. Lett. **110**, 265506 (2013).
96) A. Togo and I. Tanaka, Spglib: A Software Library for Crystal Symmetry Search (2018).
97) Web [https://github.com/atztogo/aiida-phonoxpy] (2022).
98) G. Pizzi, A. Cepellotti, R. Sabatini, N. Marzari, and B. Kozinsky, Comput. Mater. Sci. **111**, 218 (2016).
99) M. Uhrin, S. P. Huber, J. Yu, N. Marzari, and G. Pizzi, Comput. Mater. Sci. **187**, 110086 (2021).
100) Web [https://github.com/aiida-vasp/aiida-vasp] (2022).
101) A. Jain, S. P. Ong, G. Hautier, W. Chen, W. D. Richards, S. Dacek, S. Cholia, D. Gunter, D. Skinner, G. Ceder, and K. A. Persson, APL Mater. **1**, 011002 (2013).
102) A. Vaitkus, A. Merkys, and S. Gražulis, J. Appl. Crystallogr. **54**, 661 (2021).
103) M. Quirós, S. Gražulis, S. Girdzijauskaitė, A. Merkys, and A. Vaitkus, J. Cheminf. **10**, 23 (2018).
104) A. Merkys, A. Vaitkus, J. Butkus, M. Okulič-Kazarinas, V. Kairys, and S. Gražulis, J. Appl. Crystallogr. **49**, 292 (2016).
105) S. Gražulis, A. Merkys, A. Vaitkus, and M. Okulič-Kazarinas, J. Appl. Crystallogr. **48**, 85 (2015).
106) S. Gražulis, A. Daškevič, A. Merkys, D. Chateigner, L. Lutterotti, M. Quirós, N. R. Serebryanaya, P. Moeck, R. T. Downs, and A. Le Bail, Nucleic Acids Res. **40**, D420 (2012).
107) S. Gražulis, D. Chateigner, R. T. Downs, A. F. T. Yokochi, M. Quirós, L. Lutterotti, E. Manakova, J. Butkus, P. Moeck, and A. Le Bail, J. Appl. Crystallogr. **42**, 726 (2009).
108) R. T. Downs and M. Hall-Wallace, Am. Mineral. **88**, 247 (2003).
109) A. Merkys, N. Mounet, A. Cepellotti, N. Marzari, S. Gražulis, and G. Pizzi, J. Cheminf. **9**, 56 (2017).
110) A. Togo, Phonon database at Kyoto university, http://phonondb.mtl.kyoto-u.ac.jp/ (2022).
111) S. P. Ong, S. Cholia, A. Jain, M. Brafman, D. Gunter, G. Ceder, and K. A. Persson, Comput. Mater. Sci. **97**, 209 (2015).
112) A. Togo, Cogue, https://github.com/atztogo/cogue (2022).
113) L. Talirz, S. Kumbhar, E. Passaro, A. V. Yakutovich, V. Granata, F. Gargiulo, M. Borelli, M. Uhrin, S. P. Huber, S. Zoupanos, C. S. Adorf, C. W. Andersen, O. Schütt, C. A. Pignedoli, D. Passerone, J. VandeVondele, T. C. Schulthess, B. Smit, G. Pizzi, and N. Marzari, Sci. Data **7**, 299 (2020).
114) A. Togo and I. Tanaka, Phys. Rev. B **87**, 184104 (2013).

Atsushi Togo received his Ph.D. degree in 2006 from Kyoto University. After working as a post-doctoral researcher at Kyoto university, RWTH Aachen university, and CNRS, he worked as a program-specific associate professor (2012 to 2020) at ESISM, Kyoto university. Currently he is a principal researcher at National Institute for Materials Science (NIMS), Japan.